Revealing Hidden Oxygen Variability in the North Pacific: A Two-Decade Analysis Using GOBAI-O_2

Miho Ishizu[1, 2], Tomomichi Ogata[3]

[1]*Center for Climate Physics, Institute for Basic Science, Busan 46241, Republic of Korea*

[2]*Pusan National University, Tonghapgigyegwan Bldg 2 Busandaehak-ro, 63 beon-gil, Geumjeong-gu, Busan 46241, Republic of Korea*

[3]*Japan Agency for Marine-Earth Science and Technology, Environmental Variability Prediction and Application Research Group, Yokohama Institute for Earth Sciences, 3173-25 Showa-machi, Kanagawa-ku, Yokohama 236-0001, Japan*

To whom correspondence may be addressed. Email: mishizu@pusan.ac.kr

Abstract

Oceanic dissolved oxygen concentrations are thought to be declining under ongoing global warming, yet their variability remains less well understood than that of physical parameters such as temperature and salinity, primarily due to the limited spatial and temporal coverage of oxygen observation. Here, we examine linear trends in potential temperature, salinity, and dissolved oxygen in the North Pacific over the past two decades (2004–2023), using the GOBAI-O_2 dataset. We compare the diagnosed oxygen trends with those of physical parameters to reveal the spatial structure of recent changes. The oxygen trends inferred from GOBAI-O_2 are broadly consistent with trends observed along ship-based hydrographic repeat lines. While basin-scale deoxygenation is evident, we also identify localized oxygen increases on specific density surfaces. By relating these patterns to the surrounding physical

environment, we find that the spatial heterogeneity in oxygen trends is consistent with known oceanographic processes, including the southward retreat of the oxygen minimum layer and the northward migration of a front separating the subtropical and subarctic gyres. These results underscore the value of GOBAI-O_2 data in linking physical variability to previously unrecognized biological and biogeochemical patterns in the ocean.

Plain Language Summary

1. We investigated how potential temperature, salinity, and dissolved oxygen have changed in the North Pacific over the past 20 years using GOBAI-O_2 dataset, and we examined the physical processes responsible for these trends.
2. The trends identified in this study are broadly consistent with findings from previous research, and improved spatial coverage of GOBAI-O_2 allowed us to reveal connections between regional patterns that we previously only partially understood.
3. Overall, dissolved oxygen decreased across much of the North Pacific. However, some regions showed increasing oxygen levels, indicating that the changes were not uniform. These non-uniform patterns reflect known physical ocean processes. For example, higher oxygen levels in the northern North Pacific are consistent with a northward shift of the front separating the subtropical and subarctic gyres. In the equatorial Pacific, the reduced westward extent of the oxygen minimum layer corresponds to a weakening and poleward shift of the North Equatorial Countercurrent (NECC) on interdecadal timescales.
4. These findings provide new evidence that links large-scale physical ocean changes to previously unclear changes in biological and biogeochemical observations.

Keywords: dissolved oxygen, 20-year linear trends, Bio-Argo float data, global warming

1. Introduction

Over recent decades, the global ocean has experienced a decline in its dissolved oxygen inventory, a trend projected to continue through the 21st century [Keeling et al., 2010; Breitburg et al., 2018; Stramma and Schmidtko, 2021; Limburg et al., 2020; Ito et al., 2017, 2024; Kolodziejczyk et al., 2024]. This deoxygenation is driven in part by reduced ocean oxygen solubility under rising sea-surface temperatures, which promotes oxygen outgassing. In addition, enhanced stratification and a slowdown of ocean circulation under global warming can reduce interior ventilation and oxygen supply [Keeling et al., 2010; Bopp et al. 2013; Ito et al. 2017]. Ocean oxygen loss can negatively affect aerobic marine organisms [Pörtner and Farrell, 2008; Sampaio et al., 2021], alter biogeochemical cycles, and potentially induce climate-relevant feedback [Berman-Frank et al., 2008]. Historical deoxygenation has been inferred from globally distributed observations [Helm et al., 2011; Schmidtko et al., 2017; Ito et al., 2017; Takatani et al., 2012; Sasano et al., 2015; Lauvset et al., 2022b], and Earth system models have been used to simulate both historical and future changes in ocean oxygen [Bopp et al., 2013; Kwiatkowski et al., 2020; Li et al. 2020].

Observed oxygen trends have traditionally been assessed using the discrete measurements of dissolved oxygen concentration (O_2), typically obtained by Winkler titration [Winkler, 1988]. These measurements are also used to calibrate electrode- and, more recently, optode-based oxygen sensors mounted on conductivity-temperature-depth (CTD) profilers [Helm et al. 2011; Schmidtko et al., 2017; Lauvset et al., 2022b]. Although programs such as WOCE, CLIVAR, and GO-SHIP have collected high-quality oxygen measurements globally, repeat occupation intervals are commonly on the order of a decade, limiting the ability to robustly quantify annual to seasonal variability. Higher-

frequency ship-based observations exist in a few regions [Takatani et al. 2012; Sasano et al., 2015], but their spatial coverage is limited. Consequently, despite attempts to characterize basin-scale patterns [Ito et al. 2017; Stramma et al. 2020; Kolodziejczyk et al. 2024], observational constraints have hampered a spatially and temporally comprehensive understanding of dissolved oxygen variability and trends.

Oxygen sensors were first deployed on Argo profiling floats in the mid-2000s. Since then, approximately 1,800 oxygen-equipped floats have been deployed worldwide, substantially advancing the observational basis for assessing oxygen variability and trends [Sharp et al., 2023]. The expansion toward a global biogeochemical (BGC) Argo network has improved sampling in regions that were previously sparsely observed [Claustre et al., 2020]. In parallel, major progress has been made in calibration, adjustments, and quality control of oxygen measurements, including pre-deployment drift corrections [D'Asaro and McNeil, 2013; Johnson et al., 2015; Bittig and Körtzinger, 2015; Bushinsky et al., 2016; Drucker and Riser, 2016; Nicholson and Feen, 2017], climatology-based calibrations [Takeshita et al., 2013], in-air oxygen measurement calibrations [Körtzinger et al., 2005; Bittig and Körtzinger, 2015; Johnson et al., 2015; Bushinsky et al., 2016], post-deployment drift corrections [Johnson et al., 2017; Bittig et al., 2018a, b], and the standardized delayed-mode quality control procedures [Maurer et al., 2021]. Together, these developments have reduced uncertainty and improved the consistency of optode-based [O_2] measurements from Argo floats.

To date, oxygen observations from Argo floats have been used primarily in regional process studies, including air-sea oxygen exchange [Wolf et al., 2018], upper-ocean primary production [Alkire et al., 2012; Estapa et al., 2019], biological pump efficiency [Johnson and Bif, 2021], and the dynamics of the oxygen minimum zone [Udaya Bhaskar et al., 2021]. Recently, Sharp et al. [2023] produced a

four-dimensional gridded [O_2] product, GOBAI-O_2 (Gridded Ocean Biogeochemistry from Artificial Intelligence (AI) – Oxygen). GOBAI-O_2 is constructed using machine-learning methods trained on oxygen observations and designed to reconstruct spatial patterns, seasonal cycles, and decadal variability, particularly in regions where observational data gaps coincide with high background O_2 variability.

In the North Pacific, several studies have documented heterogeneous oxygen trends. Using an objectively mapped monthly climatology of O_2 based on the World Ocean Database 2013 (WOD13) [Boyer et al. 2013], Ito et al. [2017] reported multidecadal variability and trends in dissolved O_2 in the surface-layer oxygen from 1958 to 2013. Sasano et al. [2015], using the high-frequency shipboard sections along the 137°E and 165°E lines from 1987 to 2011, reported oxygen declines in the northern subtropical to subtropical-subarctic transition zones of -0.45 ± 0.16 μmol/kg/yr at 25.3 σ_θ and -0.45 ± 0.14 μmol/kg/yr at 26.8 σ_θ, respectively. They also identified a significant oxygen increase in the tropical Oxygen Minimum Layer (OML) of +0.36 ± 0.004 μmol/kg/yr, highlighting pronounced spatial heterogeneity in oxygen trends. At broader scales, Stramma et al. [2020] analyzed historical bottle data and reported links between oxygen variability and climate modes such as the Pacific Decadal Oscillation (PDO) and the North Pacific Gyre Oscillation (NPGO), although sparse sampling makes it difficult to robustly connect regional trends to physical mechanisms. Collectively, previous studies indicate that oxygen changes in the North Pacific can be strong, spatially non-uniform, and potentially driven by both circulation/ventilation changes and biologically mediated oxygen consumption [Sasano et al. 2015; 2018; Ito et al. 2017; 2024; Stramma et al., 2020; Kolodziejczyk et al. 2024].

Because observational opportunities to quantify trends in dissolved oxygen–together with concomitant changes in temperature and salinity–remain limited, gridded products such as GOBAI-O_2 are

becoming increasingly valuable for basin-scale analyses. In this study, we use GOBAI-O_2 to quantify linear trends in potential temperature, salinity, and dissolved oxygen in the North Pacific over 2004–2023 and examine how their trends are connected in both depth and density space. We further discuss the extent to which the diagnosed oxygen trends can be interpreted in terms of physical drivers, including surface warming, stratification changes, and circulation variability in the North Pacific.

2. Data and Methods

2.1 GOBAI-O_2 dataset

We use GOBAI-O_2, a four-dimensional, monthly gridded product of dissolved oxygen (O_2) in the ocean interior, generated using machine learning (ML) algorithms trained on both Argo float oxygen measurements and ship-based discrete observations [Sharp et al., 2023]. GOBAI-O_2 is mapped onto the temperature-salinity fields provided by the global Argo array [Roemmich and Gilson, 2009]. The underlying oxygen training database combines ship-based measurements from GLODAPv2.2022 and Argo float data distributed through the Argo Global Data Assembly Centers, after quality control [Sharp et al., 2023] (https://doi.org/10.25921/z72m-yz67).

According to Sharp et al. [2023], the float data used in GOBAI-O_2 were filtered to retain only delayed-mode adjusted profiles with quality flags of 1 (good), 2 (probably good), or 8 (interpolated/extrapolated) for pressure, temperature, salinity, and dissolved oxygen. Among all available float profiles, 51.4% underwent quality control through comparison with climatological fields from the World Ocean Atlas (WOA) or the Commonwealth Scientific and Industrial Research Organisation Regional Sea Atlas (CARS). An additional 30.3% were evaluated using atmospheric oxygen concentration measurements, and 7.0% were quality controlled through comparison with in-water measurements (WOD, OMS assuming an oxygen zero, or deployment-time CTD profiles). A

147 further 5.3% were adjusted using in-situ optode calibration based on the method of Drucker and Riser
148 [2016], 3.3% were adjusted by other methods, 1.9% were unclassified, and the remaining 0.9% were
149 not adjusted.

150

151 The ML models predict O_2 using predictors that include absolute salinity, conservative temperature,
152 potential density anomaly, hydrostatic pressure, bottom depth, and additional spatiotemporal
153 covariates representing geographic, seasonal, and interannual variability. Biological processes are not
154 explicitly parameterized in the ML framework; however spatiotemporal covariates can implicitly
155 capture biological influences to some extent [Giglio et al., 2018].

156

157 GOBAI-O_2 is produced using two ML approaches: feed-forward networks (FNNs) and random forest
158 regression (RFRs, [Breiman, 2001]). The final O_2 estimate at each grid point is taken as the mean
159 of the FNN and RFR predictions. The dataset spans 2004–2023 at monthly resolution on a 1° × 1°
160 latitude –longitude grid, covering 86% of the global ocean area. The product is provided on 58 vertical
161 levels from the surface to ~2,000 m. Sharp et al. [2023] reported 0.79 ± 0.04% per decade decrease
162 in the oxygen inventory of the upper 2000 m over 2004–2022. Full details of their data sources,
163 processing, algorithm training, evaluation, and uncertainty estimation are given in Sharp et al. [2023].

164

165 **2.2 Uncertainty estimates**

166 GOBAI-O_2 provides an uncertainty estimate for each gridded O_2 value, constructed by combining
167 independent uncertainty components in quadrature [Sharp et al., 2023]:

168 $$u([O_2])_{tot.} = \sqrt{u([O_2])^2{}_{meas.} + u([O_2])^2{}_{grid.} + u([O_2])^2{}_{alg.}} \quad (1),$$

169 where $u([O_2])^2{}_{meas.}$ represents measurement uncertainty of the underlying observations,

$u([O_2])^2_{grid.}$) is the gridding uncertainty associated with representing a four-dimensional spatiotemporal volume by a single value, and $u([O_2])^2_{alg.}$ is the algorithmic uncertainty arising from the ML estimation. We use $u([O_2])_{tot.}$ to characterize uncertainty in O_2 and to propagate uncertainty into our oxygen trend estimates (Figs. 1–4). In most figures, we incorporate the mean uncertainty when estimating linear O_2 trends.

2.3 Vertical grid and interpolation for isopycnal analysis

GOBAI-O_2 is provided on a 1° × 1° horizontal grid with 58 depth levels: 2.5, 10, 30, 40, 50, 60, 70, 80, 90, 100, 110, 120, 130, 140, 150, 160, 170, 182.5, 200, 220, 240, 260, 280, 300, 320, 340, 360, 380, 400, 420, 440, 462.5, 500, 550, 600, 650, 700, 750, 800, 850, 900, 950, 1000, 1050, 1100, 1150, 1200, 1250, 1300, 1350, 1412.5, 1500, 1600, 1700, 1800, 1900 and 1975 m. The enhanced near-surface vertical resolution is important for resolving strong gradients in temperature, salinity, density, and oxygen within the mixed layer [Kara et al., 2000].

For analysis performed in density space, we interpolate the original depth-level data to 1-m vertical grid using cubic spline interpolation and then evaluate linear trends on a 1° × 1° × 1 m grid. This approach enables computation of trends as a function of latitude (1° bins) and potential density anomaly (0.1σ_θ bins) (Figs. 4–7). To evaluate sensitivity to interpolation choices, we repeated the analysis using linear, shape-preserving cubic (PCHIP) interpolation and using coarser vertical grids (2 m and 5 m). The resulting trend patterns show no material differences among interpolation methods (Figs. S1 (a, b) and S2 (a, b)). The 5-m grid cannot resolve densities lighter than 24.0σ_θ at some latitudes; however, the main features are preserved across all tested resolutions.

2.4 OFES model output

In Section 3.3.2, we additionally use output from the eddy-resolving OGCM for the Earth Simulator (OFES) [Masumoto et al., 2004; 2010; Sasaki et al., 2008] to examine the physical context of the diagnosed variability. OFES is based on the MOM3 [Pacanowski and Griffies, 2000] and uses a quasi-global domain spanning 75° S– 75°N with 0.1° x 0.1° horizontal resolution and 54 vertical levels. The model was initialized from rest using the World Ocean Atlas 1998 (WOA98) [Boyer and Levitus, 1997], and spun up for 50 years using climatological forcing derived from NCEP-NCAR reanalysis [Kalnay et al., 1996]. After spin-up, a hindcast experiment was conducted from 1950 to 2024 using daily NCEP-NCAR forcing. Here we analyze OFES output over 1950–2023.

2.5 GODAS model output

In Section 3.3.2, we also use temperature and salinity fields from the NCEP Global Ocean Data Assimilation System (GODAS) to complement our analysis. GODAS is a global ocean reanalysis system developed at the National Centers for Environmental Prediction (NCEP) and is based on the Modular Ocean Model version 3 [Pacanowski and Griffes, 2000]. The system assimilates surface temperature profiles, XBT data, moored buoy observations, and other in situ measurements using a three-dimensional variational (3DVAR) assimilation scheme [Behringer and Xue, 2004; Behringer, 2007]. The GODAS reanalysis is provided on a 1° x 1° horizontal grid with enhanced meridional resolution (1/3°) near the equator and includes 40 vertical levels. The reanalysis spans from 1980 to the present and is widely used for climate diagnostics and ocean variability studies. In this study, we analyze GODAS density fields over the period 2003-2024 by using temperature and salinity.

3. Results

3.1 Horizontal distributions of linear trends

Figure 1 illustrates the horizontal and vertical distributions of linear trends in potential temperature,

salinity, and dissolved oxygen (O_2), over 2004–2023. Positive trends in potential temperature are primarily confined to the surface layer above 200 m depth (Fig. 1a–c), with larger magnitudes at higher latitudes. In contrast, negative trends emerge below the surface in the eastern tropical area (180°–120°W, 5°–15°N) (Fig. 1b), extending westward and deepening with increasing depth (Fig. 1d–f). Below ~400 m, the spatial distributions of positive and negative temperature trends differ between the subarctic and subtropical gyres.

Salinity trends exhibit generally negative values throughout the surface layer (Fig. 1h–i), consistent with freshening. Localized positive salinity trends are detected in the Kuroshio–Oyashio transition area and the northwest Pacific (140°–180°E, 20°–50°N), as well as in the tropical region (120°–170°E, 0°–10°N). Additional positive trends appear along the eastern boundary off California (130°–199°W, 20°–40°N). Below 200 m depth, salinity trends are weaker and broadly mirror the temperature ones (Fig. 1j–k). Notably, negative salinity trends are evident around the Alaska gyre (170°–130°W, 40°–55°N) (Fig. 1j–l), a pattern that differs from the corresponding temperature trends.

Negative trends in dissolved O_2 are widespread across the North Pacific and extend throughout much of the water column (Fig. 1o–u). Large negative trends are concentrated at higher latitudes near the surface, with their locations shifting systematically with depth. Particularly strong O_2 declines are observed along the northeastern boundary (140°–130°W, 40°–50°N) and within the southern subtropical region (10°–25°N) on density surfaces between 25.2 and 26.8σ_θ, corresponding to depths of approximately 200–600 m (Fig. 1q–s). In contrast, weak positive O_2 trends are detected below 200 m depth in the Kuroshio–Oyashio transition zone (130°–150°E, 30°–40°N), extending into deeper layers and spreading northeastward across the basin (Fig. 1r–u).

242 Positive O_2 trends are restricted to specific regions and depths: the tropical region at ~100 m depth
243 (Fig. 1p); the Alaska Gyre at 200–400 m depth (Fig. 1q–r); the western tropical region at 400–600
244 m depth (Fig. 1r–s); and the Kuroshio–Oyashio transition region at similar depths (Fig. 1r–s). When
245 examined as a function of latitude, the magnitudes of negative O_2 trends do not depend monotonically
246 on latitude alone. While surface-layer declines are strongest at high latitudes, the largest negative
247 trends at intermediate depths (400–600 m) occur in the mid-latitude band (30°–40°N). This depth-
248 dependent latitudinal structure implies the importance of remote transports and the circulation-driven
249 redistribution of oxygen, rather than purely local surface forcing. The underlying mechanisms are
250 discussed further in Section 3.3.

251

252 The total uncertainty in dissolved O_2, $u([O_2])_{tot.}$, exhibits pronounced regional structure (Fig. 2a–
253 g). Uncertainty is largest in the North Pacific north of 50°N and decreases toward lower latitudes.
254 Relatively high uncertainty values are also evident in the surface layer, and within regions of strong
255 density gradients in the eastern tropical Pacific [150°–120°W, 10°–30°N] at depths of 100–200 m (Fig.
256 2b–c). In general, uncertainty peaks near 100 m depth and decreases with increasing depth (Fig. 2
257 and Figure A14 in Sharp et al. [2023]). As shown by Sharp et al. [2023], regionally variations in
258 uncertainty are dominated by algorithmic uncertainty rather than measurement or gridding components
259 (Eq. 1). Elevated algorithmic uncertainty in the northern Pacific above 50°N and along the western
260 and eastern tropical margins below 20°N reflects sparse observational coverage in these regions
261 (Figure 1 in Sharp et al. 2023).

262

263 To assess whether regional trends exceed the dataset uncertainty, we computed the spatial distribution
264 of Robustness (R), defined as $R = |$ trend over two decades $|$/uncertainty (Fig. 1v–bb). This
265 diagnostic identifies regions in which the magnitude of the trend is sufficiently large to be considered

physically robust. The results indicate that R exceeds or approaches high values in the eastern and western tropical zones, the Kuroshio Extension region, portions of the subpolar North Pacific, and along the 27.2–27.4 σ_θ density surfaces at 800–1000 m depth. Based on this metric, larger oxygen trend magnitudes correspond to higher R values, indicating greater robustness. Thus, in the upper ocean (2.5–100 m), trends are physically robust mainly in the northern North Pacific. At 200–400 m, robust signals appear both in the northern North Pacific and along the 25.2–26.0 σ_θ surfaces in the southern subtropical region, as well as in the eastern and western tropics. At 600–1000 m, the trends are robust within the subtropical gyre bounded by the 27.0 σ_θ surface.

Compared with the historical horizontal distributions of dissolved O_2 reported by Ito et al. [2017] (Figure 3 in Ito et al. 2017), our analysis reveals a broader spatial extent of negative trends across the North Pacific. Whereas data gaps increase with depth in Ito et al. [2017], the GOBAI-O_2 product provides more spatially continuous coverage, yielding distributions that remain consistent with surrounding regions. In addition, positive O_2 trends detected here in the Kuroshio–Oyashio transition zone and the northeastern North Pacific on density surfaces of 26.8–27.0σ_θ (Fig. 1r) were not clearly evident in the earlier climatology-based analysis. Similarly, the positive trends identified in the western tropical Pacific below 400 m depth (Fig. 1r–t) are stronger and more spatially coherent than those reported previously.

The positive O_2 trends coincide with regions of relatively low uncertainty values (Fig. 1p–s and 1w–y), suggesting that they are robust features supported by the high observation density of Argo profiling floats. Other regions exhibiting positive signals—the northeastern North Pacific with a density range of 26.8–27.0σ_θ (170°E–150°W, 45–55°N, Fig. 1r) and the tropical western Pacific (130°–170°E, 0°–

10°N, Fig. 1r–t)—also correspond to areas of low uncertainty (Fig. 1y–aa). Consequently, these signals likely represent genuine regional reoxygenation superimposed on the basin-scale deoxygenation trend.

Some localized expansions of the trend patterns, particularly in the tropical eastern Pacific (e.g. 170°–130°W, 0°–20°N) may partly reflect regions of elevated uncertainty, occasionally exceeding 15 μmol/kg (Fig. 1q–s; Fig. 4i). Such large uncertainties arise from sparse observations and high background variability [Sharp et al. 2023]. Additional bias may stem from sensor calibration limitations in Argo oxygen measurements, especially in oxycline regions where finite optode response times can introduce systematic errors [Bittig et al., 2014; 2018a,b]. Despite these caveats, the spatial patterns of the diagnosed O_2 trends are generally smooth and coherent across the basin. Based on statistical significance testing, most trends are significant throughout the water column (Fig. 1o–u), allowing them to be interpreted in the context of established physical processes in the North Pacific. Overall, the GOBAI-O_2 dataset provides an improved framework for diagnosing basin-scale oxygen variability and its physical drivers.

3.2 Vertical sections and isopyncal density analysis of linear trends in 137°E and 165°E lines

To facilitate direct comparison with historical ship-based observations, we examine vertical sections and isopycnal distributions of linear trends in potential temperature, salinity, and dissolved O_2 along the 137°E and 165°E meridional sections (Fig. 3). Ogata and Nonaka [2020] analyzed salinity data from 20 years of shipboard observations along the 137°E line between 1997 and 2016, while Sasano et al. [2015] analyzed temperature, salinity, and dissolved O_2 data from 25 years of cruises along the 165°E line between 1987 and 2011.

312

313 Along both sections, large negative trends in potential temperature and salinity are concentrated along
314 the 25.0–26.0σ_θ isopycnal surfaces, corresponding to potential temperatures of approximately 10–
315 12°C and salinities of 34.4–34.5 (Fig. 3a, b, e, f). In contrast, the strongest negative trends in dissolved
316 O_2 occur primarily along denser isopycnals between 26.0 and 27.0σ_θ (Fig. 3c, g). This vertical
317 separation indicates that the regions of pronounced oxygen decline are not co-located with those of
318 temperature and salinity trends, implying distinct controlling mechanisms.

319

320 In addition to widespread oxygen declines, pronounced positive O_2 trends are detected south of ~15°N
321 below 200 m depth along the 137°E line (Fig. 3c). These positive trends are located near the upper
322 boundary of the oxygen minimum layer (OML). Comparison with the corresponding uncertainty
323 distributions (Fig. 3d, h) shows that regions exhibiting positive or negative oxygen trends generally
324 do not coincide with areas of elevated uncertainty, indicating that these signals are robust within the
325 GOBAI-O_2 framework.

326

327 The distributions of linear trends on isopycnal surfaces further highlight differences among
328 temperatures, salinity, and dissolved O_2 (Fig. 4). Trends in temperature and salinity are closely aligned,
329 with warming accompanied by salinification and cooling accompanied by freshening (Fig. 4a–b, d–
330 e). In the tropical region (5°S–5°N), distinct positive trends in both variables are evident over the
331 density range of 22.0–26.0σ_θ. In contrast, little systematic trend is detected in the salinity minimum
332 region (S = 34–34.1) within the density range of 26.5–27.0σ_θ. At higher latitudes (40°–50°N), strong
333 positive trends in both temperature and salinity are observed along the 26.0–27.0σ_θ surfaces (Fig. 4e).

334

335 Dissolved oxygen trends exhibit a markedly different structure. Although negative O_2 trends dominate

336 overall, weak but coherent positive trends appear across the density range 23.0–26.0σ_θ in low-latitude
337 regions (5°S–5°N). More pronounced positive O_2 trends are detected in the deeper density range of
338 26.0–27.0σ_θ between 5° and 10°N. Additional weak positive trends are observed between 10° and
339 20°N within the density range of 23.0–25.0σ_θ along both the 137°E and 165°E sections.

340

341 Compared with previous studies, the GOBAI-O_2-based trends reveal both similarities and notable
342 differences. The general characteristics of temperature and salinity trends are broadly consistent with
343 those reported by Sasano et al. [2015], although the present results are spatially smoother, particularly
344 for dissolved oxygen. This smoothness likely reflects the gridded nature of the dataset and the spatial
345 regularization inherent in the machine-learning reconstruction. Along the 137°E section, the GOBAI-
346 O_2 temperature and salinity fields exhibit a wider area of negative salinity trends within the density
347 range 22.0–24.0 σ_θ than those reported by Ogata and Nonaka [2020] using OFES output.

348

349 Ship-based observations by Sasano et al. [2015] identified patchy positive trends in oxygen within
350 the density range 24.5–27.5σ_θ in the regions (5°–15°N and 6°S–1°N), as well as localized positive
351 trends at greater depths. In contrast, the GOBAI-O_2 data reveal a broader, smoother, and more spatially
352 coherent pattern of positive O_2 trend spanning 6°S to 5°N. At the same time, the present analysis more
353 clearly delineates the core regions of negative oxygen trends between 5° and 15°N along the lower
354 isopycnals (Fig. 3c and f), which are characteristic of the subtropical gyre. These differences
355 underscore the complementary nature of ship-based observations and gridded reconstructions and
356 highlight the advantage of GOBAI-O_2 for resolving basin-scale and isopycnal-scale oxygen variability.

357

358 **3.3 Horizontal distribution of linear trends along isopycnal surfaces**

359 **3.3.1 Potential temperature and salinity**

The horizontal distributions of linear trends in potential temperature, salinity, and dissolved oxygen on specific isopycnal surfaces at 25.0, 26.0, and 26.8σ_θ (Fig. 5) are illustrated to examine how these trends occur and how they are connected. These density surfaces correspond to the shallower density range of Subtropical Mode Water (STMW), the shallower densities of Central Mode Water (CMW) [Suga et al., 1997; 2004], and the representative density of North Pacific Intermediate Water (NPIW) [Nakamura et al., 2000a, b; Nakamura and Awaji, 2003; Yasuda, 2004], respectively. STMW is formed south of the Kuroshio Extension between 30–35°N and 130–170°E, and reaches depths of approximately 400 m in late winter. It then spreads toward the subtropical front through advection across the Kuroshio recirculation area. CMW is formed in the transition area of the central North Pacific and spreads eastward along the North Pacific Current before turning southward and westward in the subtropical gyre [Suga et al., 1997; 2004]. In contrast, NPIW does not outcrop during its formation process. Its origin lies in Okhotsk Sea Mode Water, which forms through overturning driven by diapycnal upwelling and tidal mixing around the Kuril Islands [Nakamura et al., 2000a, b; Nakamura and Awaji, 2003; You, 2003; Yasuda, 2004] as well as double diffusions in the North Pacific [You, 2003].

The linear trends on the 25.0, 26.0, and 26.8σ_θ surfaces show that positive and negative tendencies appear in characteristic locations and are generally aligned with the geostrophic streamlines (Fig. 5a–b, d–e, g–h). Although exceptions exist, such as weak positive trends (150–175°E, 20–30°N) (Fig. 5a–b), negative trends in potential temperature and salinity dominate in the western and central North Pacific on the 25.0 and 26.0σ_θ surfaces (Fig. 5a–b, d–e). Conversely, positive trends in temperature and salinity are most prevalent in the northeastern and/or eastern regions of the basin along the geostrophic streamlines (Fig. 5a–b, d–e). These patterns suggest that waters subducted in the frontal region with reduced temperature and salinity originate mainly from the northeastern North Pacific and are advected southward along the subtropical circulation (Fig. 5a–b, d–e). Exceptions occur in parts

of the northeastern basin (170–130°W, 40–60°N), where warmer and more saline waters influence the water masses sinking near the Alaska gyre and subsequently transported outside the subtropical gyre and along the California coast.

At $26.8\sigma_\theta$ (Fig. 5g–h), large positive trends in temperature and salinity are found along the Kuril Islands, with moderate positive trends appearing on the eastern side of the basin, respectively. Waters at this density range ($26.8\sigma_\theta$) are not directly ventilated but are formed through diapycnal mixing processes [Nakamura et al., 2000a, b; Nakamura and Awaji, 2003; You, 2003; Yasuda, 2004] and through double diffusion such as salt fingering [You, 2003]. Thus, the observed positive temperature and salinity trends at $26.8\sigma_\theta$ likely reflect influences from changes occurring in the overlying layers (Fig. 5d–e and g–h).

A meridional northward shift of the outcrop line in the North Pacific associated with recent climate change has been documented in OFES analyses [Ogata and Nonaka, 2020] and in other observational, reanalysis, and eddy-resolving ocean hindcasts [Xu et al., 2022]. Consistent with these studies, the present dataset exhibits clear northward migration of the $25.0\sigma_\theta$ and $26.0\sigma_\theta$ outcrop lines (Fig. 6a), with the strong shifts occurring in the eastern basin between 150°E and 180°W (Fig. 6 and Table 1). The estimated northward shift rate at 0.004–0.09 $°yr^{-1}$ from 2004 to 2023 is comparable to the value of 0.04 $°yr^{-1}$ reported by Xu et al. [2022] for 1980 to 2018. Xu et al. [2022] further demonstrated that changes in the mixed layer and outcrop lines are tightly coupled with the northward migration of the North Pacific subtropical gyre and KE/OE fronts due to the poleward expansion of the Hadley cell, including the fact that the Kuroshio Extension and Oyashio Extension fronts, mode waters, and subtropical fronts evolve as a coherent system. These changes may also reflect the influence of anthropogenic warming, which has been linked to the poleward expansion of the Hadley circulation

and the associated meridional shifts of oceanic fronts [Yang et al., 2020].

Such poleward displacements of frontal structures can help explain the negative temperature and salinity trends in the subtropical gyre, where less saline subarctic-origin waters are subducted and advected southward. The positive temperature and salinity trends occurring in the Alaska region [160°–130°W, 30°–60°N] (Fig. 5a–b and d–e) are likewise consistent with the direct surface warming. In contrast, the 26.0σ_θ front exhibits primarily longitudinal, rather than meridional, shifts between 2004 and 2023 (Fig. 6), suggesting that the associated temperature and salinity changes arise mainly from direct surface warming and freshening, rather than from density-compensated shifts in water-mass distribution.

3.3.2 Dissolved oxygen

The linear trends in dissolved oxygen on the isopycnal surfaces at 25.0, 26.0, and 26.8σ_θ exhibit predominantly negative values across the North Pacific (Fig. 5c, f, and i), although their spatial distributions are not uniform. Large negative trends are concentrated in the northeastern and eastern regions and gradually decrease toward the west (Fig. 5c, f, and i). Exceptions occur mainly in the tropics, where notable positive trends are found in the western tropical areas on the 26.0 and 26.8σ_θ surfaces.

The temporal changes in dissolved oxygen (O_2) were decomposed following the method of Sasano et al. [2015]. The processes underlying the oxygen tendency equations (Eqs. 2 and 3) are summarized below. We evaluated each contributing term and examined its relative importance for the dissolved O_2 trends. The total tendency of dissolved oxygen can be expressed as

$$\frac{\partial O_2}{\partial t} = \left(\frac{\partial O_2}{\partial z}\frac{\partial z}{\partial t}\right) + \left(\frac{\partial O_2^{sat}}{\partial t}\right)_{net} - \left(\frac{\partial (AOU)}{\partial t}\right)_{net}, \quad (2)$$

which can be rearranged as

$$\frac{\partial O_2}{\partial t} = \left(\frac{\partial O_2}{\partial z}\frac{\partial z}{\partial t}\right) + \left(\frac{\partial O_2^{sat}}{\partial t} - \frac{\partial O_2^{sat}}{\partial z}\frac{\partial z}{\partial t}\right) + \left(-\frac{\partial (AOU)}{\partial t} + \frac{\partial (AOU)}{\partial z}\frac{\partial z}{\partial t}\right). \quad (3)$$

(i) (ii) (iii) (iv) (v) (vi)

Here, $X = O_2$, O_2^{sat}, AOU (Apparent Oxygen Utilization). The term $\partial z/\partial t$ denotes the temporal change in the depth of the isopycnal surface (z), while $\partial X/\partial z$ represents the vertical gradient of the variable X at that surface, averaged over the past 20 years. The net tendency term ($\partial X/\partial t$)$_{net}$ represents the net changes associated with a variable X.

By applying Eq. (3), the rate of O_2 change (term i), which is the rate of reconstructed O_2 data estimated from the linear regression analysis, on each isopycnal surface can be decomposed into contributions from:

(term ii) vertical heave acting on the vertical O_2 gradient;

(term iii) solubility effects due to temperature and salinity changes;

(term iv) vertical heave acting on the solubility gradient;

(term v) AOU changes related to air-sea disequilibrium, biological activities, and lateral circulation

(term vi) vertical heave acting on AOU gradients.

The derivation of Eqs. (2) and (3) follows Sasano et al. [2015] and is described in Appendix. A schematic illustration of this decomposition is provided in Supplementary Figure S5.

Figure 7 shows the horizontal distributions of the magnitude of each term on 25.0, 26.0, and 26.8σ_θ surfaces. The results indicate that the prominent O_2 declines (Fig. 5c, f, i) arise from a combination of positive and negative contributions, with the dominant terms varying by latitude. In the high-latitude region around the Alaska Gyre (170°–130°W, 40°–60°N), the largest negative contributions are associated with the deepening of isopycnal surfaces (term ii) and the vertical heave acting on the AOU gradient (term vi) (Fig. 7f, j, k, o). Because the dissolved oxygen generally decreases with depth ($\partial O_2/\partial z < 0$), deepening of isopycnal surfaces ($\partial z/\partial t > 0$) (Fig. 8 b–c) produces a negative contribution through vertical heave. Similarly, because AOU typically increases with depth, isopycnal deepening leads to an apparent increase in AOU, contributing negatively to dissolved O_2 via term (vi). In contrast, solubility-related changes (term iii) and net AOU tendencies (term v) act in opposite directions during this period (Fig. 7g–h, l–m). Taken together, these results are consistent with the strong negative O_2 trends observed in the Bering Sea on the 26.0$\sigma_\theta$and 26.8σ_θ surfaces (150°E–170°W, 50–60°N; Figs. 5f and i).

In the subtropical and mid-latitudes (10°–40°N), the O_2 decline is largely associated with AOU changes (term v) (Fig. 7d, i, and n). The relative weakening of the total O_2 decrease in the western North Pacific (Fig. 5c, f, i) coincides with positive contributions from vertical heave of isopycnal surfaces (term ii) (Fig. 7f and k). Additional positive trends arise from solubility-related effects (term iii) (Fig. 7b), and the vertical heave acting on the AOU gradient (term vi) (Fig. 7j and o and Fig. 8b–c).

In the mid-ocean between 170°E and 160°W, the positive O_2 tendencies transition to weakly negative values. In contrast, a pronounced band of positive trends is found zonally across the North Pacific

475 Ocean between 30°N and 50°N, primarily associated with the combined effects of terms (iii) and (v)
476 (Fig. 7l, h–i, and m–n). This pattern may be related to the northward meridional shift of the subtropical
477 and subarctic frontal zone under recent global warming [Ogata and Nonaka, 2020]. Enhanced winter
478 convection in this region may introduce nutrients into the surface layer, potentially increasing
479 biological activity and AOU. In the NPIW formation region near the Kuril Islands, negative
480 contributions from term (iii) are observed (Fig. 7l), suggesting weaker vertical mixing during the
481 observational period, likely influenced by enhanced surface-layer stratification. This interpretation is
482 supported by the positive trends in temperature and salinity observed in the winter subducted areas
483 [Suga et al., 1997; 2004; Yasuda, 2004] (Fig. 5d–e, g–h).

484

485 In the western tropical Pacific, pronounced increases in dissolved O_2 are observed within the density
486 range of 26.8–27.2 σ_θ (Fig. 3c and g; Fig. 4c and g; Fig. 5c, f, and i), overlapping with the OML
487 [Reid, 1997]. Similar features have been reported by Sasano et al. [2015] and Takatani et al. [2012].
488 Variability of the North Equatorial Counter Current (NECC) is likely relevant in this region.
489 According to the study of Chen et al. [2016] based on the OFES outputs including a multidecadal
490 variability (1960–2014), the NECC exhibits two distinct modes of variability: an interannual mode
491 characterized by strengthening accompanied by southward migration, and an interdecadal mode
492 marked by a gradual weakening, poleward migration, and broadening.

493

494 The validity of time-varying signals in the western tropical Pacific in the OFES data has been
495 demonstrated by Chen et al. [2016]. We further examined the longer-term OFES data (1950–2023),
496 as well, for poleward, eastward velocities, as well as potential temperature and salinity here (Fig. 9c,
497 g). Positive temperature anomalies in 0°–5 °N occur above 250 m depth, while negative anomalies

498 appear along the 26.0σ_θ surface between 5°–20°N, a similar pattern that is also evident in the GOBAI-
499 O_2 data (Fig. 3a). A discrepancy is found in salinity trends: GOBAI-O_2 shows negative trends along
500 26.0σ_θ (Fig. 3b), whereas OFES exhibits positive trends (Fig. 9b, f), likely reflecting higher salinity
501 at 200–600 m depth in OFES between 0° and 7°N (Fig. 10b, d).

502

503 Anomalies in poleward and eastward velocities (Fig. 9a–b, e–f and Fig. 11a–b) indicate enhanced
504 poleward flow around 5°N above 200m depth and a poleward shift of the eastward velocity core. These
505 changes are consistent with the interdecadal mode of NECC variability described by Chen et al.
506 [2016]. The broadening of the NECC was less evident here, possibly because the present analysis
507 uses raw velocity fields rather than isolating the second EOF modes. The wind-stress curl over the
508 equatorial Pacific shows a persistent decrease and poleward expansion of negative values along the
509 0°–10°N from 1950 to 2023 (Fig. 12).

510

511 The westward penetration of the OML is slow and occurs between two eastward-extending tongues of
512 high O_2 water originating near the equator [Reid, 1997] (Fig. S6). The observed O_2 increase on the
513 26.8–27.2 σ_θ surfaces (Fig. 3c, g and Fig. 4c, g) is consistent with a weakening and northward shift
514 of the interdecadal NECC mode. The subsurface O_2 increase, particularly below 400m depth (Fig. 1r–
515 u), is therefore likely influenced by these circulation changes, potentially allowing higher-O_2 water to
516 extend westward (Fig. S6). In addition, shoaling of isopycnal surfaces near the equator indicates a
517 northward shift of the boundary between the tropical and subtropical gyres along 137°E line during
518 the observational period.

519

4. Discussion and Conclusion

The variability of dissolved oxygen in the North Pacific reflects the combined influences of global warming and climate variability. In this study, we used the four-dimensional GOBAI-O_2 dataset, constructed using machine–learning methods applied to historical temperature, salinity, and oxygen observations from BGC-Argo floats and ship-based measurements–to examine linear trends in potential temperature, salinity, and dissolved oxygen over the past two decades (2004–2023). The linear trends are broadly consistent with findings from previous studies [Takatani et al. 2012; Sasano et al. 2015; Ogata and Nonaka, 2020], and we clarified how these trends vary spatially (Figs. 3 and 4).

An important outcome of this study is that GOBAI-O_2, being globally gridded, allows spatially continuous and smooth representations of trends, both horizontally and vertically, across the North Pacific. This provides a more coherent picture than earlier datasets that relied solely on sparse ship-based observations. The horizontal trend patterns mapped on isopycnal surfaces (Fig. 5) show that dissolved oxygen exhibits a basin-scale decreasing trend. At the same time, several regions display locally increasing oxygen, including areas influenced by the meridional migration of subtropical and subpolar fronts (Fig. 4). The strong positive oxygen trends in the western equatorial region are consistent with a weakening of the second mode of the NECC variability. The decomposition analysis further illustrates how each physical component contributes to oxygen changes along isopycnal surfaces (Fig. 7).

Although many of the large-scale features identified here resemble those reported by Ito et al. [2017], our analysis reveals regional and isopycnal-scale structures that were previously unresolved. In particular, the positive oxygen trends in the Kuroshio–Oyashio Transition Zone, the northeastern North

Pacific along the 26.8–27.0 σ_θ density surfaces, and the enhanced subsurface O_2 increase in the tropical western Pacific below 400 m were not clearly distinguished in earlier climatology-based studies. These improvements arise because GOBAI-O_2 integrates high-frequency BGC-Argo oxygen observations with a spatially consistent mapping scheme, reducing observational gaps and sampling biases in dynamically active regions. This demonstrates that regional reoxygenation signals can coexist with large-scale deoxygenation, and highlights the importance of sustained BGC-Argo observations for detecting emerging changes in ocean biogeochemistry.

Recent work by Bushinsky et al. [2025] has reported the presence of a systematic negative bias (approximately -2.7 μmol kg^{-1}) in air-calibrated BGC-Argo oxygen measurements compared with ship-based reference profiles. This bias does not appear to be explicitly corrected in the GOBAI-O_2 and may therefore influence the magnitude of the estimated oxygen trends–potentially enhancing negative trends or suppressing positive ones in regions with dense float sampling. However, as described in Section 2.1, a substantial fraction of these float data is subject to quality control through comparison with climatological fields derived from ship-based discrete observations, and only profiles with appropriate quality flags are retained and incorporated into the dataset development. This filtering procedure likely mitigates a portion of the air-calibration bias.

If present, such biases could also affect the apparent vertical structure of the oxycline. In the North Pacific, regions with high float density–such as the Kuroshio–Oyashio transition zone, the North American coastal region, and the vicinity of Hawaii–may be particularly affected (see Fig. 1 of Sharp et al., 2023). While a constant offset would not directly alter linear trend estimates, any time–varying bias associated with sensor behavior or sampling depth could introduce spurious trends. A quantitative evaluation is not feasible at present due to the lack of temporally continuous ship-based reference data

568 at the spatial scales. This limitation should therefore be kept in mind when interpreting the O_2 trends
569 reported here.

570

571 It is also essential to recognize that GOBAI-O_2 is a machine learning reconstruction derived from
572 available temperature, salinity, and oxygen measurements. While this approach significantly enhances
573 spatial coverage, the results should be interpreted cautiously. Importantly, however, such
574 methodological uncertainties are unlikely to alter the large-scale spatial coherence of the trend patterns
575 identified in this study. Nevertheless, future work incorporating improved calibration of Argo oxygen
576 sensors, expanded ship-based reference datasets, independent machine learning reconstructions [e.g.,
577 Ito et al., 2024], and comprehensive ocean reanalysis will be necessary to better constrain these
578 uncertainties.

579

580 The monthly mean climatological GOBAI-O_2 data set should include the Pacific Decadal Oscillation
581 (PDO; Stramma et al., 2020; Pozo Buil and Di Lorenzo, 2017) and the North Pacific Gyre Oscillation
582 (NPGO; Stramma et al., 2020). This dataset, therefore, provides a valuable basis for examining how
583 such climate variability influences dissolved oxygen through physical driving mechanisms.
584 Investigating these relationships more explicitly will be an important direction for future research.

585

586

587 **Data availability:**

588 GOBAI-O_2 data is available at https://www.ncei.noaa.gov/access/metadata/landing-
589 page/bin/iso?id=gov.noaa.nodc:0259304. Temperature and salinity are from Roemmich and Gilson
590 [2009] Argo climatology (https://sio-argo.ucsd.edu/RG_Climatology.html). The OFES, NCEP-
591 NCAR, and GODAS data used in our study are obtained from APDRC, University of Hawaii
592 (http://apdrc. soest.hawaii.edu).

Author contributions:

MI designed the study, performed the analyses, and prepared all figures. MI wrote the initial draft of the manuscript. MI and TO contributed to the interpretation of the results. All authors contributed to improving the manuscript.

Acknowledgements:

Jonathan D. Sharp and the reviewers are acknowledged for providing comments that prompted significant improvements to this manuscript.

Financial support:

This research has been supported by the Institute for Basic Science (grant no. IBS-R028-D1) and the Japan Society for the Promotion of Science (JSPS) through a Grant-in-Aid for Scientific Research JP22H00176.

Table captions:

Table 1. Northern shifts of the (outcrop) isopycnal latitudes (° yr^{-1}) for 25.0σ_θ (a), 26.0σ_θ (b), and 26.8σ_θ (c) in the GOBAI-O_2, OFES, and GODAS datasets. The estimates are based on data from March of each year. For 26.8 σ_θ, the northern shift is evaluated using the isopycnal depths corresponding to 182, 178m, and 183m in GOBAI-O2, OFES, and GODAS, respectively.

(a) 25.0σ_θ

Longitude	GOBAI-O_2	OFES	GODAS
150 °E	0.0241	0.0157	0.0283
170 °E	0.0444	0.0052	0.0240
170 °W	0.0684	0.0871	0.0481
150 °W	0.0947	0.0353	0.0313
130 °W	0.0420	0.0471	0.0121

(b) 26.0σ_θ

Longitude	GOBAI-O_2	OFES	GODAS
150 °E	0.0368	0.0766	0.0358
170 °E	0.0436	-0.0305	0.0508
170 °W	0.0124	0.1997	0.1412

(c)26.8σ_θ

Longitude	GOBAI-O_2	OFES	GODAS
150 °E	0.0371	0.1980	0.0046
170 °E	0.0338	0.0217	0.1637
170 °W	0.0728	0.0054	0.0261

Figure captions:

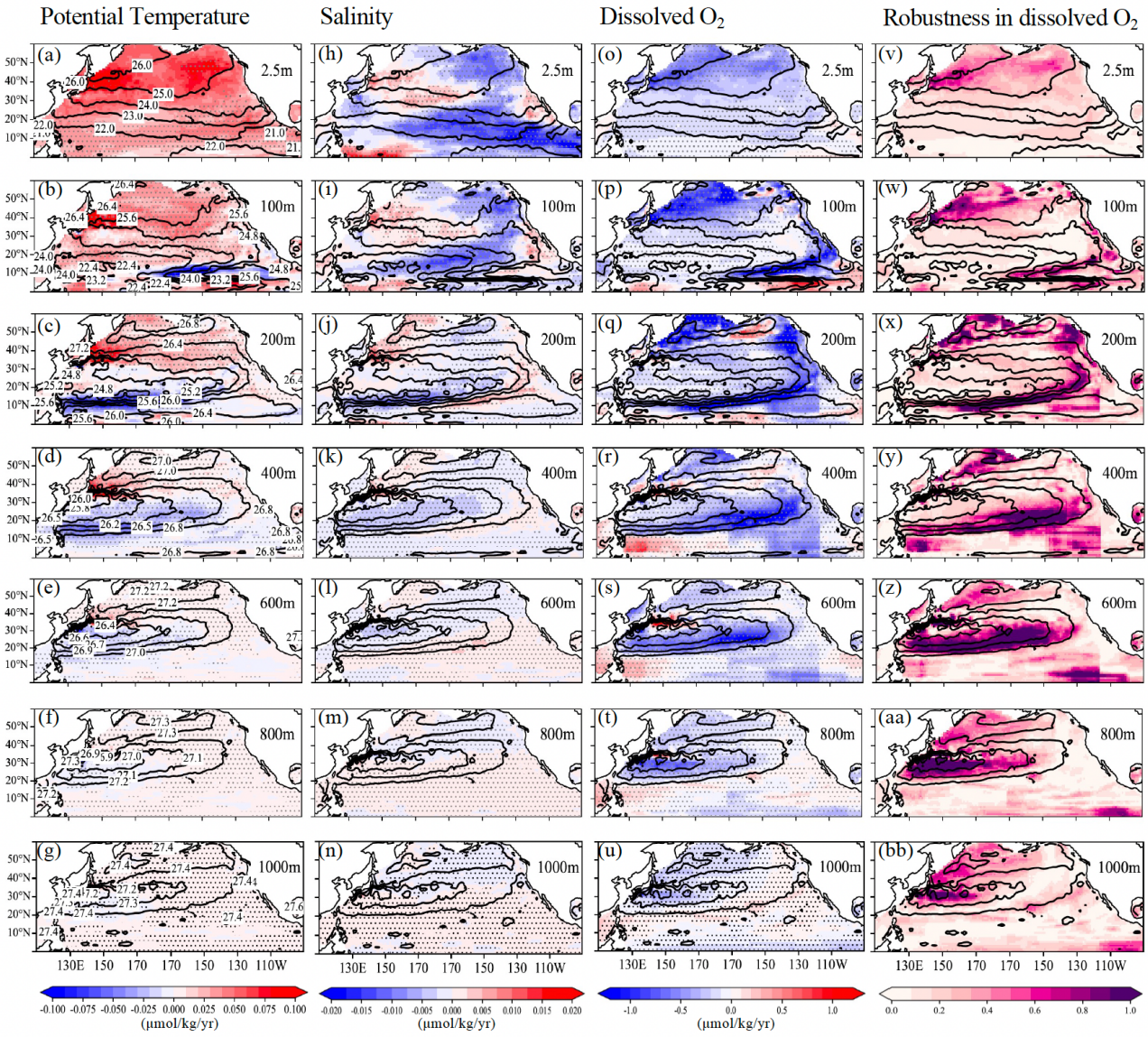

Figure 1 Horizontal distributions of linear trends (μmol/kg/yr) in (a–g) potential temperature, (h–n) salinity, and (o–u) dissolved oxygen (O_2) during the observational period at depths of 0, 100, 200, 400, 600, 800, and 1000 m, respectively. Hatched areas indicate statistically significant trends at the 95% confidence level based on a Student's t-test with effective degrees of freedom accounting for temporal autocorrelation. Trend significance was evaluated using a Student's t-test with effective degrees of freedom accounting for lag-1 autocorrelation. Contours denote potential density at each depth. Labels for the potential density are shown only in the potential temperature sections. Corresponding distributions of the Robustness (R) , defined as the ratio of the trend magnitude to the dataset uncertainty in dissolved O_2 are presented in panels (v–bb).

640

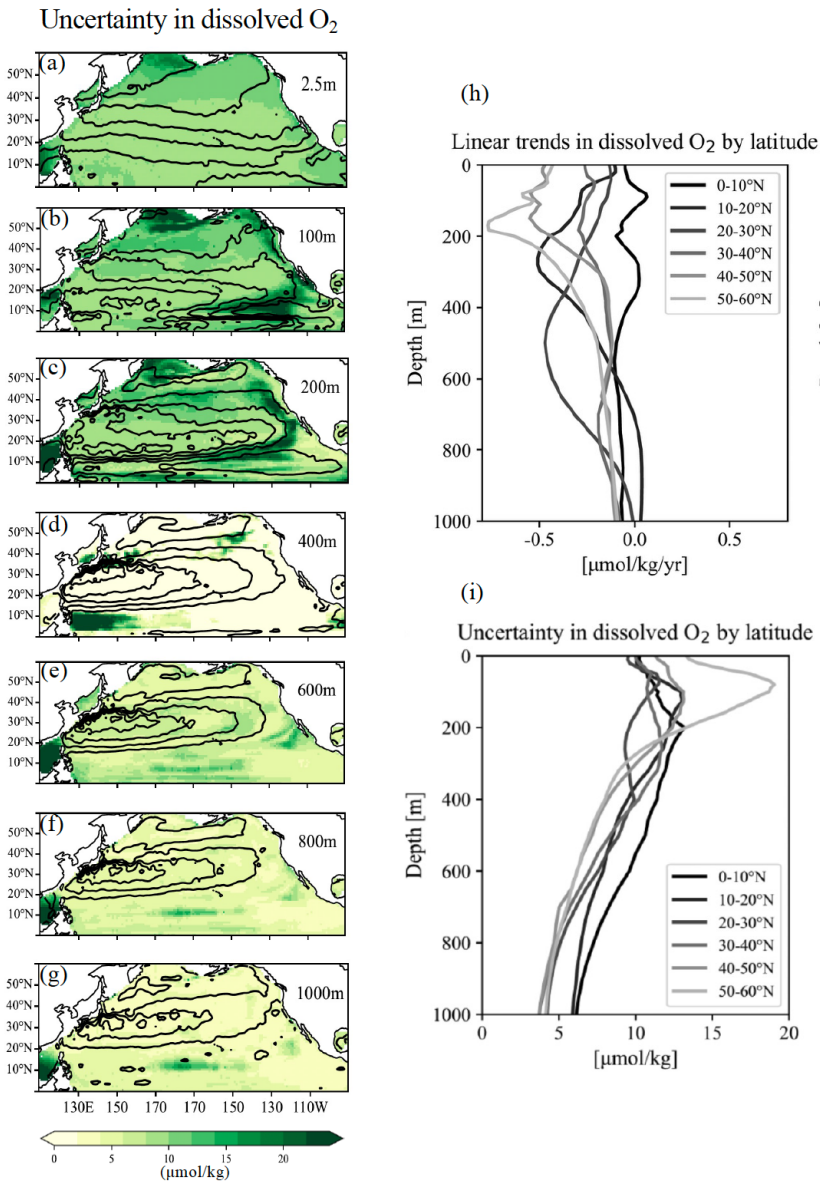

641

642 **Figure 2** Horizontal distributions of dataset uncertainty in dissolved O_2 (a–g) and vertical profiles of

643 linear trends and uncertainty in dissolved O_2 by latitude (h–i).

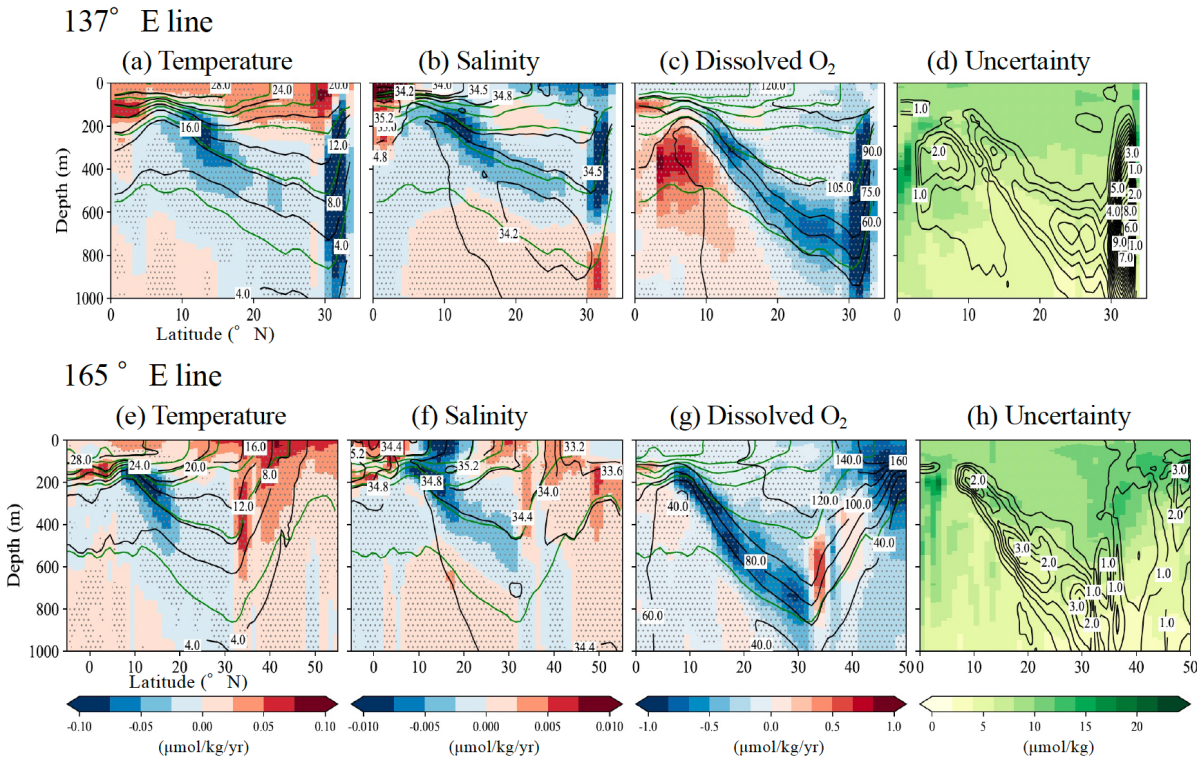

644

645 **Figure 3** Vertical sections showing linear trends in potential temperature (a, e), salinity (b, f), and
646 dissolved O_2 (c, g) along the 137°E and 165°E meridians, respectively. Black contour lines indicate
647 the mean potential temperature (a, f), salinity (b, g), and dissolved oxygen (c, h) over the period
648 2004–2023, while green contour lines represent the mean potential density. Labels for the potential
649 density are shown only in the robustness sections. Hatched areas indicate statistically significant trends
650 at the 95% confidence level based on a Student's t-test with effective degrees of freedom accounting
651 for temporal autocorrelation. Trend significance was evaluated using a t-test with effective degrees of
652 freedom accounting for lag-1 autocorrelation. Corresponding vertical sections of the mean uncertainty
653 with the contours of the Robustness (R) in panels (d, h).

654

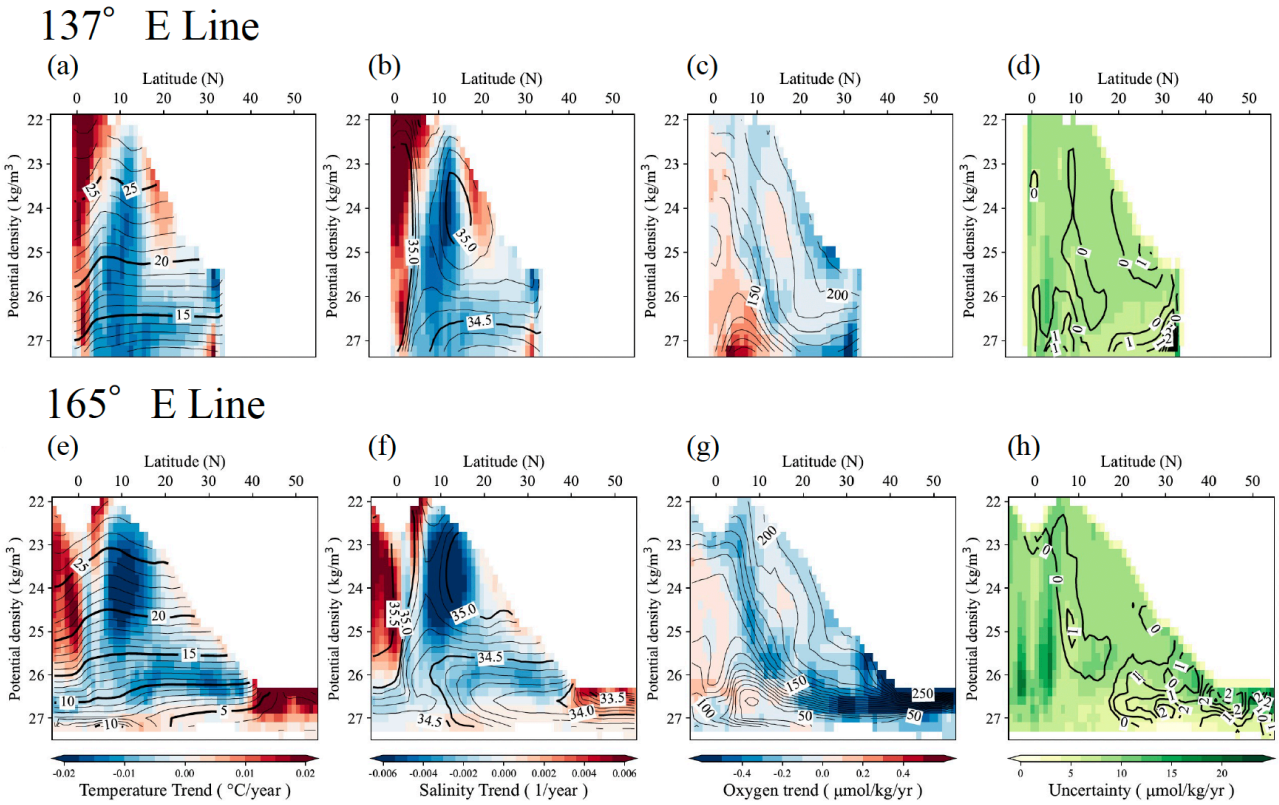

Figure 4 Linear trends in (a, e) potential temperature, (b, f) salinity, (c, g), and dissolved O_2 on each isopycnal surface at intervals of $0.1\sigma_\theta$, calculated at every 1.0 deg of latitude in 137 °E and 165 °E lines, respectively. Contour lines represent the mean values during the target observation periods, plotted at intervals of $0.1\sigma_\theta$ for each 1 degree of latitude. Panels (d, h) show the corresponding vertical sections of mean uncertainty, along with contours of robustness (R).

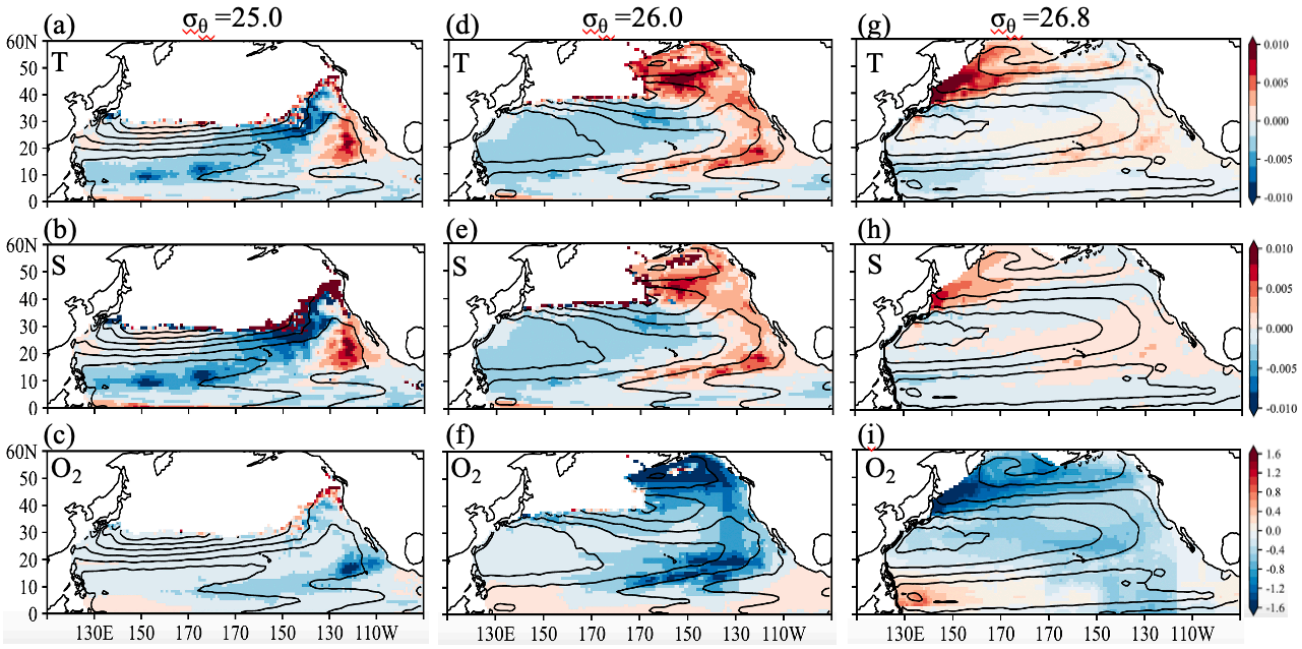

662

663 **Figure 5** Linear trends in (a) potential temperature, (b) salinity, and (c) dissolved O_2 on each
664 isopycnal surface at 25.0, 26.0, and 26.8σ_θ. Contour lines represent geostrophic flow streamlines on
665 26.0 and 26.8σ_θ surfaces, relative to 2000 m.

666

667

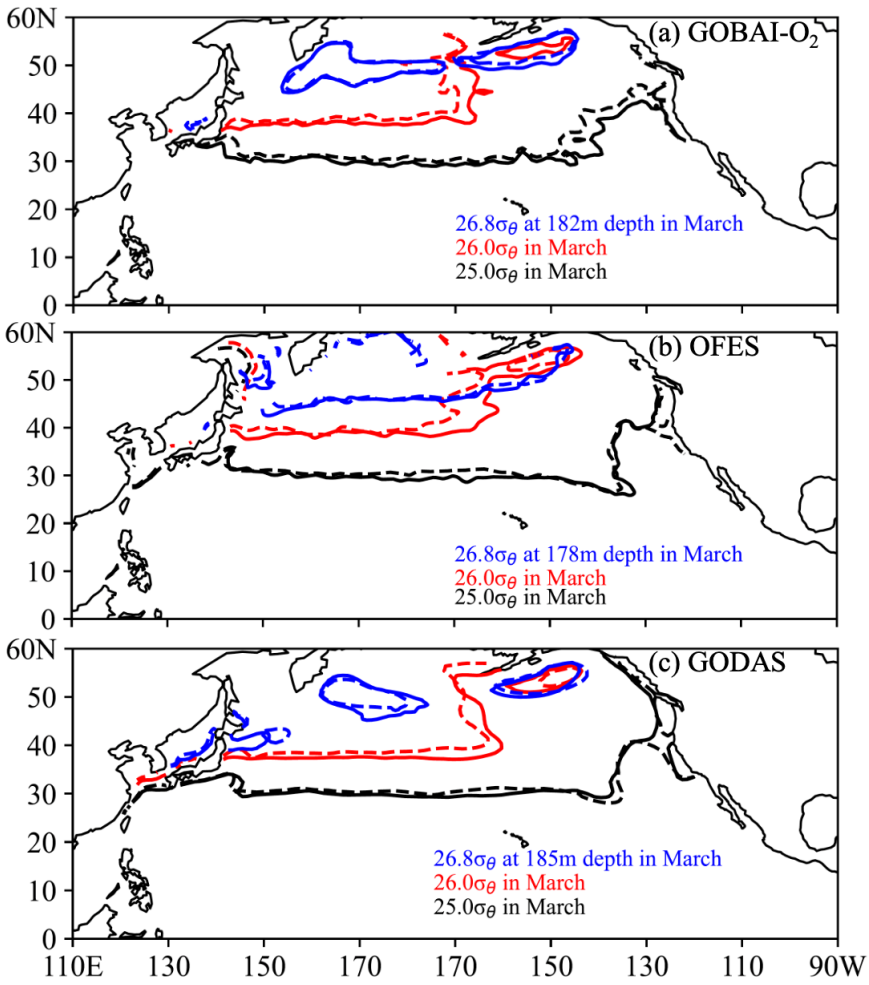

668

669 **Figure 6** Density contours of 25.0σθ (black), 26.0σθ (red), and 26.8σθ (blue) in each dataset: (a)
670 GOBAI-O_2, (b) OFES, and (c) GODAS. Solid lines indicate the mean March density contours for
671 2004–2009, while dashed lines represent those for 2019–2023.

672

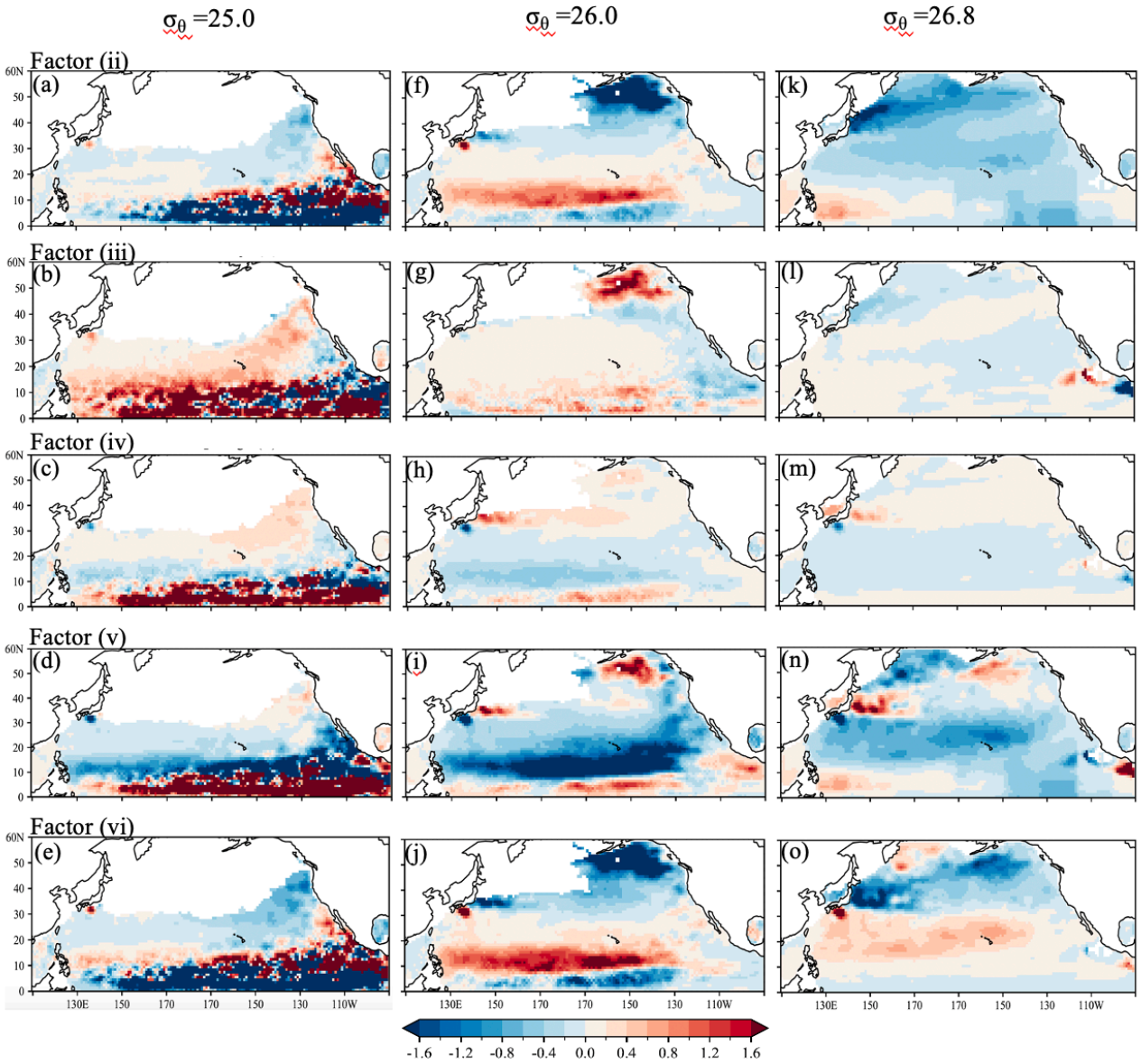

673

674 **Figure 7** Horizontal distributions of the magnitude of each factor contributing to the rate of O_2 change
675 on 25.0, 26.0, and 26.8 σ_θ in Eq. (1). The rate of O_2 change on each isopycnal surface is decomposed
676 into the following components: (ii) the apparent contribution from vertical heave (deepening or
677 shoaling) of isopycnal surfaces associated with warming and/or surface freshening; (iii) the
678 contribution from changes in oxygen solubility (O_2^{sat}) associated with temperature and salinity
679 variations; (iv) the contribution from vertical heave acting on the background solubility gradient;
680 (v) the contribution from net changes in apparent oxygen utilization (AOU) associated with air–sea
681 disequilibrium, biological activity, and lateral advection and/or circulation; and (vi) the contribution
682 from vertical heave acting on AOU gradients, independent of solubility changes. This decomposition
683 is applied to the reconstructed dissolved oxygen fields obtained from linear regression analysis.

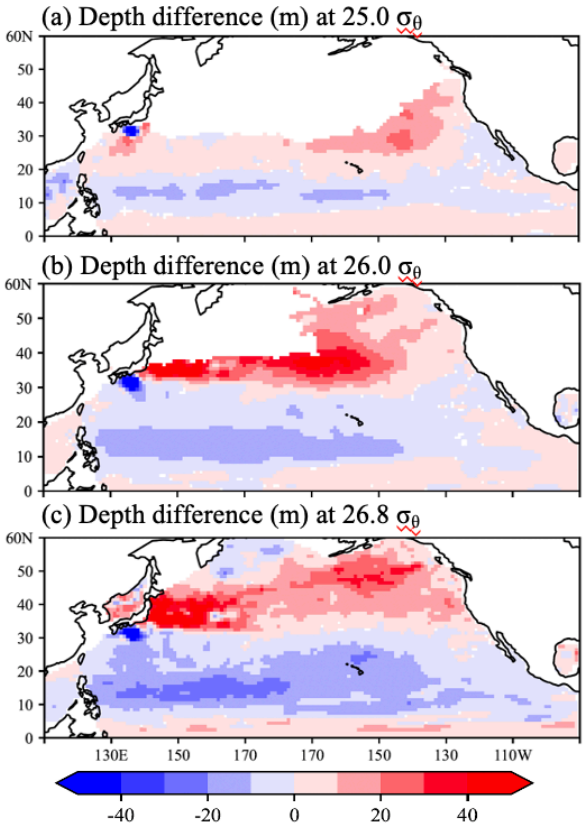

Figure 8 Depth difference (m) between the 5-year averaged data in March, 2004–2009 and 2018–2023 at 25.0, 26.0, and 26.8σ_θ. The reconstructed O_2 data estimated from the linear regression analysis were used in this calculation. Positive and negative values indicate the deepening and shallowing, respectively, from the depth of each density in 2004–2023.

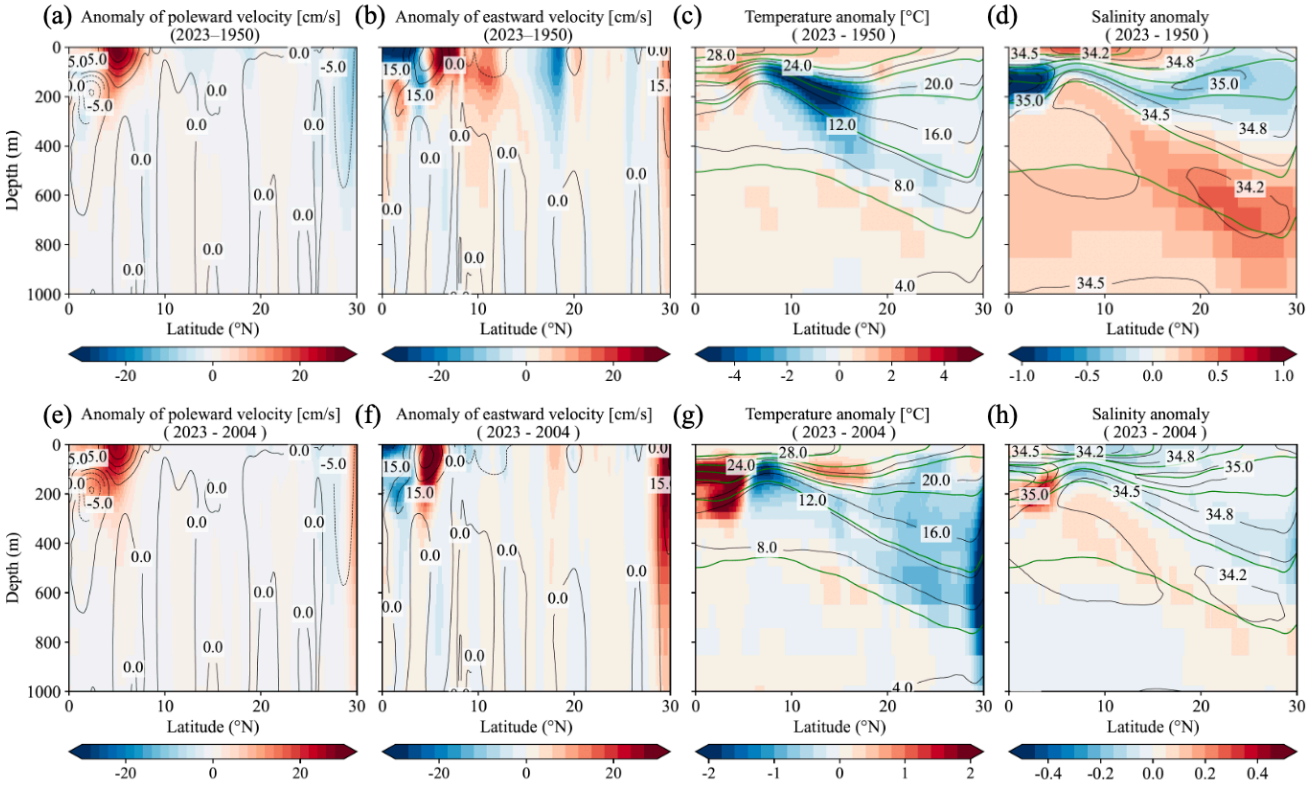

691

692 **Figure 9.** Anomaly of poleward and eastward velocity, potential temperature, and salinity in the OFES
693 model outputs from 1950 to 2023 (a–d) and from 2004 to 2023 (e–h), respectively, in the 137°E line.
694 Contours of averaged values of poleward and eastward velocity, potential temperature, and salinity
695 during the target period are also shown in each figure. Green contour lines in (c–d, g–h) indicate the
696 average potential density of 22, 23, 24, 25, 26, and 27σ_θ, during the target periods.

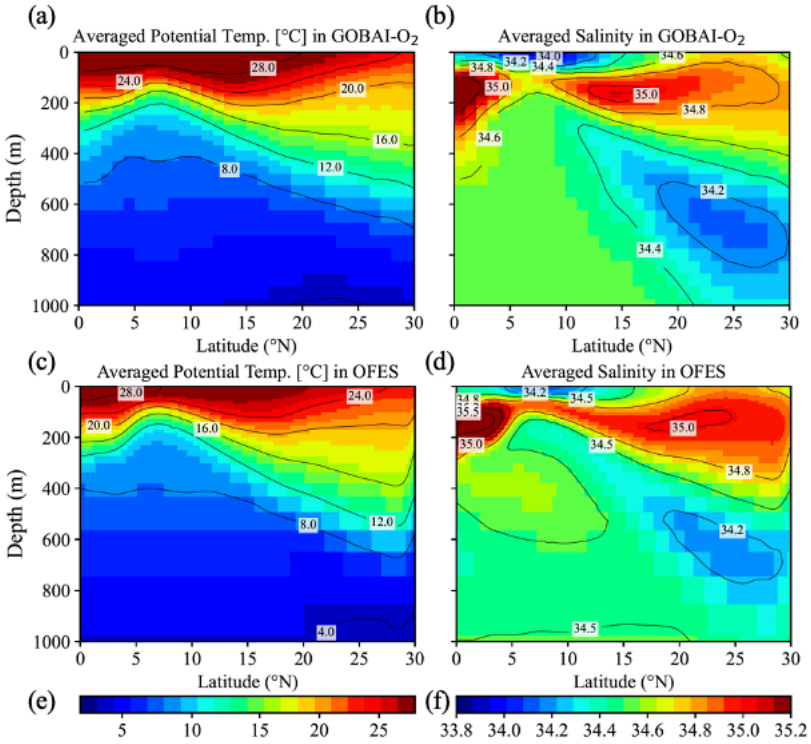

Figure 10. Averaged Potential Temperature (a, c) and salinity (b, d) in GOBAI-O_2 from 2004 to 2023 and OFES data from 1950 to 2023, respectively, in the 137°E line.

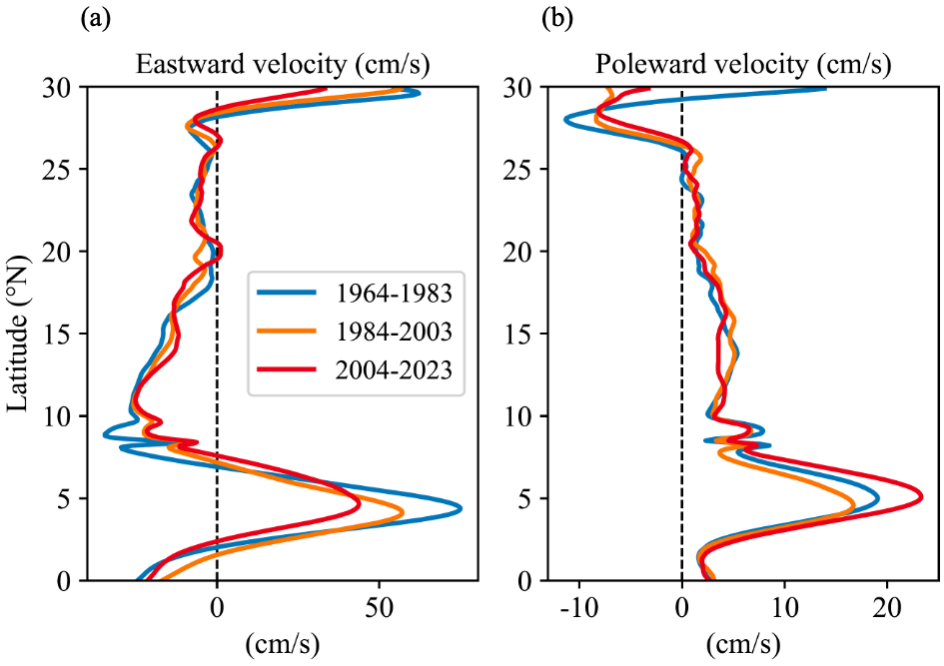

Figure 11. Latitudinal distribution of averaged eastward (a) and poleward velocity (b) in the OFES data from 1964 to 1983, from 1984 to 2003, and from 2004 to 2023, respectively, in the 137°E line.

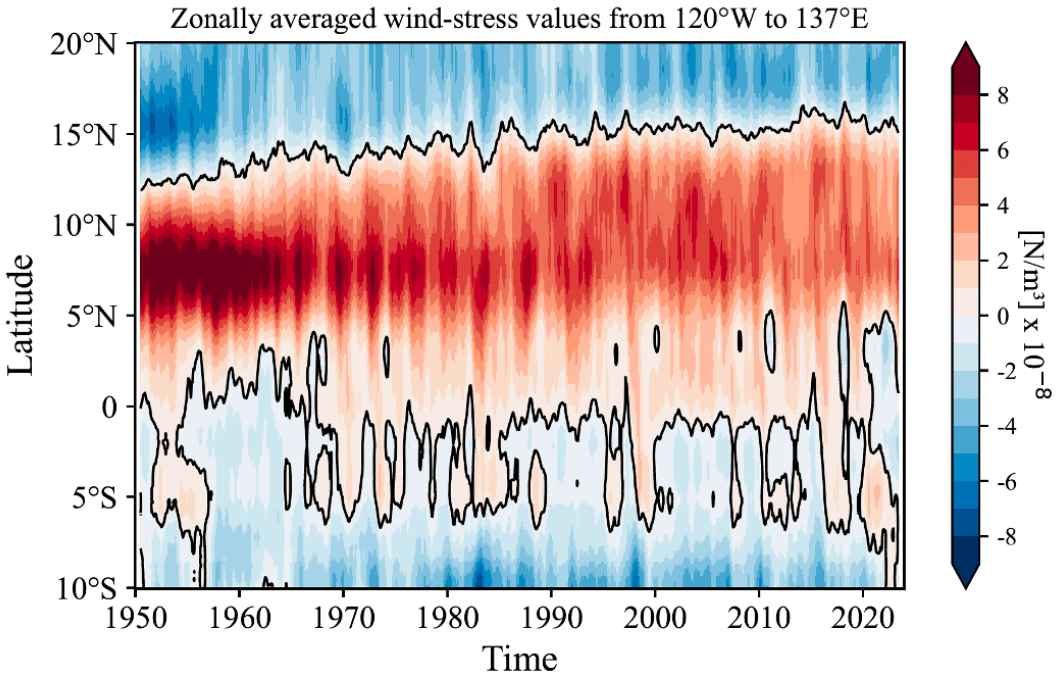

704

705 **Figure 12.** NCEP-NCAR wind-stress curl values zonally averaged from 137°E to 120° W from 1950
706 to 2023. A 13-month running-mean filter has been applied in time.

707

708 **Appendix: Essential concepts and derivations for Equation (2–3)**

709 The essential concepts and derivations for equations (2) and (3) were originally proposed by Takatani
710 et al. [2012] and subsequently described in detail by Sasano et al. [2015]. Here, we briefly summarize
711 and follow their derivation.

712

713 When the temperature at a depth z_A increases from θ_A to θ_A' as a result of increased ocean heat
714 content, the density at that depth decreases from σ_A to σ_A'. For simplicity, the vertical salinity profile
715 is assumed to remain unchanged with time. As a consequence, the isopycnal surface of σ_A deepens
716 from z_A to z_B (Figure S5). If surface freshening occurs simultaneously due to a net freshwater input,
717 both the density decreases at z_A (from σ_A to σ_A') and the deepening of the isopycnal surface (from
718 z_A to z_B) are enhanced. Because density is a function of temperature and salinity ($\sigma = f(\theta, S)$), the

719 density of the isopycnal surface σ_A can be expressed as

720 $$\sigma_A = f(\theta_A, S_A) \quad \text{(before warming)} \quad \text{(C1)}$$

721 $$= f(\theta_B', S_B). \quad \text{(after warming)} \quad \text{(C2)}$$

722 Here, S_A and S_B denote salinity at depth z_A and z_B, respectively, and θ_B' represents the temperature at
723 density σ_A at depth z_B after warming. The depth z_B is determined by satisfying Eqs. (C1) and (C2).
724 In the region where salinity decreases with depth (e.g., above the salinity minimum layer of NPIW),
725 $S_A > S_B$, and therefore $\theta_A > \theta_B'$. This implies that the potential temperature on an isopycnal surface
726 effectively decreases as a consequence of warming, and that biogeochemical properties on the same
727 isopycnal surface are also expected to change.

728

729 For a tracer X whose vertical profile with respect to depth does not change with time (e.g., salinity;
730 see Figure S5 (c)), the temporal change of X on the potential density surface σ_A is attributed solely
731 to the apparent change caused by the deepening of the isopycnal surface from z_A to z_B:

732 $$\frac{\partial X}{\partial t} = \left(\frac{\partial X}{\partial z} \cdot \frac{\partial z}{\partial t}\right) \quad \text{(C3)}$$

733 Here, $\partial X/\partial t$ represents the temporal change of X observed on σ_A (gray arrows in Figure S5), z
734 denotes the depth of σ_A, $\partial X/\partial z$ is the vertical gradient of X with respect to the depth (assumed to be
735 time-invariant), and $\partial z/\partial t$ is the rate of deepening of the isopycnal surface σ_A. The product
736 $\partial X/\partial z \cdot \partial z/\partial t$ represents the effect of isopycnal deepening (white arrows in Figure S5),
737 corresponding to the difference between the filled square and filled circle.

738

739 For a variable Y whose vertical profile evolves with time while warming occurs simultaneously, the
740 temporal change of Y on the density surface σ_A can be expressed as the sum of two components: the
741 contribution due to the isopycnal deepening from z_A to z_B and the net temporal change of Y,

742 ($\partial Y/\partial t$)$_{net}$ between the time before and after warming:

743 $$\frac{\partial Y}{\partial t} = \left(\frac{\partial Y}{\partial z} \cdot \frac{\partial z}{\partial t}\right) + \left(\frac{\partial Y}{\partial t}\right)_{net} \qquad (C4)$$

744 To evaluate the net change ($\partial Y/\partial z$)$_{net}$ (illustrated by the blue arrows of a difference in symbols
745 between filled square and open square in Figure S5), it is necessary to evaluate the contribution of the
746 temporal change of *Y* due to the isopycnal deepening and to subtract it from the change of *Y* observed
747 at density σ_A. For instance, the change of O_2^{sat} in Figure S5 (f) is observed along the gray isopycnal
748 surface (large white arrow), whereas the net change (large blue and pink arrows) is obtained as the
749 difference between the observed change and the deepening effect.

750

751 The dissolved oxygen concentration O_2 can be expressed as:

752 $$O_2 = O_2^{sat} - AOU, \qquad (C5)$$

753 where O_2^{sat} is the oxygen saturation concentration (a function of temperature and salinity), and AOU
754 is "apparent oxygen utilization", representing the oxygen consumed by biological processes since
755 subduction. Near the surface, AOU is typically small, and its contributions can be neglected.

756

757 Following Eq. (C4), the temporal change of O_2 on a given isopycnal surface at a fixed station is:

758 $$\frac{\partial O_2}{\partial t} = \left(\frac{\partial O_2}{\partial z} \cdot \frac{\partial z}{\partial t}\right) + \left(\frac{\partial O_2}{\partial t}\right)_{net}. \qquad (C6)$$

759 Similarly,

760 $$\frac{\partial O_2^{sat}}{\partial t} = \left(\frac{\partial O_2^{sat}}{\partial z} \cdot \frac{\partial z}{\partial t}\right) + \left(\frac{\partial O_2^{sat}}{\partial t}\right)_{net}, \qquad (C7)$$

761 and

762 $$\frac{\partial AOU}{\partial t} = \left(\frac{\partial (AOU)}{\partial z} \cdot \frac{\partial z}{\partial t}\right) + \left(\frac{\partial (AOU)}{\partial t}\right)_{net}. \qquad (C8)$$

763 The term $_{net}$ is directly related to warming, because depends on temperature and salinity. If AOU does
764 not change with time, that is, if changes in O_2 arise solely from changes in, then $\partial(AOU)/\partial t$ follows
765 Eq. (C3) and $= 0$. If AOU varies with time, however, $\partial(AOU)/\partial t$ follows Eq. (C4) and $\neq 0$, as
766 illustrated by the dashed gray line in Figure S5 (g).

767

768 Because O_2 is defined by Eq. (C5), the net temporal change of O_2 on an isopycnal surface is

769 $$\left(\frac{\partial O_2}{\partial t}\right)_{net} = \left(\frac{\partial O_2^{sat}}{\partial t}\right)_{net} - \left(\frac{\partial (AOU)}{\partial t}\right)_{net}. \qquad \text{(C9)}$$

770 Combining Eqs. (C6) and (C9), the total temporal change of O_2 on an isopycnal surface can be
771 written as

772 $$\left(\frac{\partial O_2}{\partial t}\right) = \left(\frac{\partial O_2}{\partial z}\cdot\frac{\partial z}{\partial t}\right) + \left(\frac{\partial O_2^{sat}}{\partial t}\right)_{net} - \left(\frac{\partial (AOU)}{\partial t}\right)_{net}, \qquad \text{(C10)}$$

773 which corresponds to Eq. (1) in the main text. Eq. (C10) corresponds to an arrow in Figure S5 (e),
774 represented from left to right by the large gray arrow, white, blue, and pink arrows. The large blue
775 arrow is identical to Figure S5 (f), while the large pink arrow corresponds to Figure S5(g), but with
776 its direction reversed. Finally, substituting Eqs. (C7) and (C8) into (C10)

777 $$\frac{\partial O_2}{\partial t} = \left(\frac{\partial O_2}{\partial z}\frac{\partial z}{\partial t}\right) + \left(\frac{\partial O_2^{sat}}{\partial t} - \frac{\partial O_2^{sat}}{\partial z}\frac{\partial z}{\partial t}\right) - \left(\frac{\partial (AOU)}{\partial t} - \frac{\partial (AOU)}{\partial z}\frac{\partial z}{\partial t}\right), \text{ (C11)}$$

778 (i) (ii) (iii) (iv) (v) (vi)

779 which corresponds to Eq. (2) in the main text. Note: The signs in terms (v) and (vi) in Eq. (3) are
780 reversed relative to those in Eq. (C11) for convenience.

781

782 Table A1 The physical interpretation of each term in the oxygen tendency decomposition shown in Eq.
783 (3) and Eq. (C11) is summarized.

Term	Mathematical form	Physical interpretation
(ii)	$(\partial O_2/\partial z)(\partial z/\partial t)$	Vertical heave acting on the O_2 gradient
(iii)	$\partial O_2^{sat}/\partial t$	Solubility effect due to temperature and salinity changes
(iv)	$-(\partial O_2^{sat}/\partial z)(\partial z/\partial t)$	Vertical heave acting on the solubility gradient
(v)	$\partial AOU/\partial t$	AOU changes related to air–sea disequilibrium, biological activity and lateral circulation
(vi)	$-(\partial AOU/\partial z)(\partial z/\partial t)$	Vertical heave of the AOU gradient

784

785

786 **References:**

787 Alkire, M. B., D'Asaro, E., Lee, C., Jane Perry, M., Gray, A., Cetinić, I., et al. (2012). Estimates of
788 net community production and export using high-resolution, Lagrangian measurements of O2, NO3−,
789 and POC through the evolution of a spring diatom bloom in the North Atlantic. *Deep Sea Research*
790 *Part I: Oceanographic Research Papers*, *64*, 157–174. https://doi.org/10.1016/j.dsr.2012.01.012
791 Behringer, D. W., & Xue, Y. (2004). Evaluation of the global ocean data assimilation system at NCEP:
792 The Pacific Ocean. 8th Symposium on Integrated Observing and Assimilation Systems for Atmosphere,
793 Oceans, and Land Surface, AMS 84th Annual Meeting, Washington State Convention and Trade Center,
794 Seattle, Washington, 11-15. https://ams.confex.com/ams/pdfpapers/70720.pdf
795 Behringer, D. W. (2007). The Global Ocean Data Assimilation System (GODAS) at NCEP. 11th
796 Symp. on Integrated Observing and Assimilation Systems for Atmosphere, Oceans, and Land
797 Surface, San Antonio, TX, Amer. Meteor. Soc., 3.3. [Available online
798 at https://ams.confex.com/ams/pdfpapers/119541.pdf.]
799 Berman-Frank, I., Lundgren, P., & Falkowski, P. (2003). Nitrogen fixation and photosynthetic oxygen
800 evolution in cyanobacteria. *Research in Microbiology*, *154*(3), 157–164.
801 https://doi.org/10.1016/S0923-2508(03)00029-9

Bittig, H. C., Fiedler, B., Scholz, R., Krahmann, G., & Körtzinger, A. (2014). Time response of oxygen optodes on profiling platforms and its dependence on flow speed and temperature. *Limnology and Oceanography: Methods*, *12*(8), 617–636. https://doi.org/10.4319/lom.2014.12.617

Bittig, H. C., & Körtzinger, A. (2015). Tackling Oxygen Optode Drift: Near-Surface and In-Air Oxygen Optode Measurements on a Float Provide an Accurate in Situ Reference. https://doi.org/10.1175/JTECH-D-14-00162.1

Bittig, H. C., Körtzinger, A., Neill, C., van Ooijen, E., Plant, J. N., Hahn, J., et al. (2018a). Oxygen Optode Sensors: Principle, Characterization, Calibration, and Application in the Ocean. *Frontiers in Marine Science*, *4*. https://doi.org/10.3389/fmars.2017.00429

Bittig, H. C., Steinhoff, T., Claustre, H., Fiedler, B., Williams, N. L., Sauzède, R., et al. (2018b). An Alternative to Static Climatologies: Robust Estimation of Open Ocean CO_2 Variables and Nutrient Concentrations From T, S, and O_2 Data Using Bayesian Neural Networks. *Frontiers in Marine Science*, *5*. https://doi.org/10.3389/fmars.2018.00328

Bopp, L., Resplandy, L., Orr, J. C., Doney, S. C., Dunne, J. P., Gehlen, M., et al. (2013). Multiple stressors of ocean ecosystems in the 21st century: projections with CMIP5 models. *Biogeosciences*, *10*(10), 6225–6245. https://doi.org/10.5194/bg-10-6225-2013

Boyer, T. P., and S. Levitus (1997), Objective Analyses of Temperature and Salinity for the World Ocean on a 1/48 Grid, vol. 11, NOAA Atlas NESDIS, Natl. Oceanic and Atmos. Admin., Silver Spring, Md.

Boyer, T. P., Antonov, J. I., Baranova, O. K., Coleman, C., Garcia, H. E., Grodsky, A., et al. (2013). World Ocean Database 2013. Retrieved from https://repository.oceanbestpractices.org/handle/11329/357

Breiman, L. (2001). Random Forests. *Machine Learning*, *45*(1), 5–32. https://doi.org/10.1023/A:1010933404324

826 Breitburg, D., Levin, L. A., Oschlies, A., Grégoire, M., Chavez, F. P., Conley, D. J., et al. (2018).
827 Declining oxygen in the global ocean and coastal waters. *Science*, *359*(6371), eaam7240.
828 https://doi.org/10.1126/science.aam7240
829 Bushinsky, S. M., Emerson, S. R., Riser, S. C., & Swift, D. D. (2016). Accurate oxygen measurements
830 on modified Argo floats using in situ air calibrations. *Limnology and Oceanography: Methods*, *14*(8),
831 491–505. https://doi.org/10.1002/lom3.10107
832 Bushinsky, S.M., Nachod, Z., Fassbender, A.J., Tamsitt, V., Takeshita, Y., Williams, N., 2025. Offset
833 Between Profiling Float and Shipboard Oxygen Observations at Depth Imparts Bias on Float pH and
834 Derived pCO2. Global Biogeochemical Cycles 39, e2024GB008185.
835 https://doi.org/10.1029/2024GB008185
836 Chen, X., Qiu, B., Du, Y., Chen, S., & Qi, Y. (2016). Interannual and interdecadal variability of the
837 North Equatorial Countercurrent in the Western Pacific. *Journal of Geophysical Research: Oceans*,
838 *121*(10), 7743–7758. https://doi.org/10.1002/2016JC012190
839 Claustre, H., Johnson, K. S., & Takeshita, Y. (2020). Observing the Global Ocean with
840 Biogeochemical-Argo. *Annual Review of Marine Science*, *12*(Volume 12, 2020), 23–48.
841 https://doi.org/10.1146/annurev-marine-010419-010956
842 D'Asaro, E. A., & McNeil, C. (2013). Calibration and Stability of Oxygen Sensors on Autonomous
843 Floats. https://doi.org/10.1175/JTECH-D-12-00222.1
844 Drucker, R., & Riser, S. C. (2016). In situ phase-domain calibration of oxygen Optodes on profiling
845 floats. *Methods in Oceanography*, *17*, 296–318. https://doi.org/10.1016/j.mio.2016.09.007
846 Estapa, M. L., Feen, M. L., & Breves, E. (2019). Direct Observations of Biological Carbon Export
847 From Profiling Floats in the Subtropical North Atlantic. *Global Biogeochemical Cycles*, *33*(3), 282–
848 300. https://doi.org/10.1029/2018GB006098

Giglio, D., Lyubchich, V., & Mazloff, M. R. (2018). Estimating Oxygen in the Southern Ocean Using Argo Temperature and Salinity. *Journal of Geophysical Research: Oceans*, *123*(6), 4280–4297. https://doi.org/10.1029/2017JC013404

Helm, K. P., Bindoff, N. L., & Church, J. A. (2011). Observed decreases in oxygen content of the global ocean. *Geophysical Research Letters*, *38*(23). https://doi.org/10.1029/2011GL049513

Ito, T., Minobe, S., Long, M. C., & Deutsch, C. (2017). Upper ocean O_2 trends: 1958–2015. *Geophysical Research Letters*, *44*(9), 4214–4223. https://doi.org/10.1002/2017GL073613

Ito, T., Cervania, A., Cross, K., Ainchwar, S., & Delawalla, S. (2024). Mapping Dissolved Oxygen Concentrations by Combining Shipboard and Argo Observations Using Machine Learning Algorithms. *Journal of Geophysical Research: Machine Learning and Computation*, *1*(3), e2024JH000272. https://doi.org/10.1029/2024JH000272

Johnson, K. S., Plant, J. N., Riser, S. C., & Gilbert, D. (2015). Air Oxygen Calibration of Oxygen Optodes on a Profiling Float Array. https://doi.org/10.1175/JTECH-D-15-0101.1

Johnson, K. S., Plant, J. N., Coletti, L. J., Jannasch, H. W., Sakamoto, C. M., Riser, S. C., et al. (2017). Biogeochemical sensor performance in the SOCCOM profiling float array. *Journal of Geophysical Research: Oceans*, *122*(8), 6416–6436. https://doi.org/10.1002/2017JC012838

Johnson, K. S., & Bif, M. B. (2021). Constraint on net primary productivity of the global ocean by Argo oxygen measurements. *Nature Geoscience*, *14*(10), 769–774. https://doi.org/10.1038/s41561-021-00807-z

Kalnay, E., Kanamitsu, M., Kistler, R., Collins, W., Deaven, D., Gandin, L., et al. (1996). The NCEP/NCAR 40-Year Reanalysis Project. Retrieved from https://journals.ametsoc.org/view/journals/bams/77/3/1520-0477_1996_077_0437_tnyrp_2_0_co_2.xml

872 Kara, A. B., Rochford, P. A., & Hurlburt, H. E. (2000). An optimal definition for ocean mixed layer
873 depth. *Journal of Geophysical Research: Oceans*, *105*(C7), 16803–16821.
874 https://doi.org/10.1029/2000JC900072
875 Keeling, R. F., Körtzinger, A., & Gruber, N. (2010). Ocean Deoxygenation in a Warming World.
876 *Annual Review of Marine Science*, *2* (Volume 2, 2010), 199–229.
877 https://doi.org/10.1146/annurev.marine.010908.163855
878 Kolodziejczyk, N., Portela, E., Thierry, V., & Prigent, A. (2024). ISASO2: recent trends and regional
879 patterns of ocean dissolved oxygen change. *Earth System Science Data*, *16*(11), 5191–5206.
880 https://doi.org/10.5194/essd-16-5191-2024
881 Körtzinger, A., Schimanski, J., & Send, U. (2005). High Quality Oxygen Measurements from Profiling
882 Floats: A Promising New Technique. https://doi.org/10.1175/JTECH1701.1
883 Kwiatkowski, L., Torres, O., Bopp, L., Aumont, O., Chamberlain, M., Christian, J. R., et al. (2020).
884 Twenty-first century ocean warming, acidification, deoxygenation, and upper-ocean nutrient and
885 primary production decline from CMIP6 model projections. *Biogeosciences*, *17*(13), 3439–3470.
886 https://doi.org/10.5194/bg-17-3439-2020
887 Lauvset, S. K., Lange, N., Tanhua, T., Bittig, H. C., Olsen, A., Kozyr, A., et al. (2022b).
888 GLODAPv2.2022: the latest version of the global interior ocean biogeochemical data product. *Earth*
889 *System Science Data*, *14*(12), 5543–5572. https://doi.org/10.5194/essd-14-5543-2022
890 Li, C., Huang, Jianping, Ding, L., Liu, X., Yu, H., Huang, Jiping, 2020. Increasing Escape of Oxygen
891 From Oceans Under Climate Change. Geophysical Research Letters 47, e2019GL086345.
892 https://doi.org/10.1029/2019GL086345
893 Limburg, K. E., Breitburg, D., Swaney, D. P., & Jacinto, G. (2020). Ocean Deoxygenation: A Primer.
894 *One Earth*, *2*(1), 24–29. https://doi.org/10.1016/j.oneear.2020.01.001
895 Masumoto, Y., Sasaki, H., Kagimoto, T., Komori, N., Ishida, A., Sasai, Y., et al. (2004). A fifty-year
896 eddy-resolving simulation of the world ocean: Preliminary outcomes of OFES (OGCM for the Earth

Simulator). Journal of the Earth Simulator, 1,35–56. https://www.jamstec.go.jp/ceist/j/publication/journal/jes_vol.1/pdf/JES1-3.2-masumoto.pdf

Masumoto, Y. (2010). Sharing the results of a high-resolution ocean general circulation model under a multi-discipline framework—a review of OFES activities. *Ocean Dynamics*, *60*(3), 633–652. https://doi.org/10.1007/s10236-010-0297-z

Maurer, T. L., Plant, J. N., & Johnson, K. S. (2021). Delayed-Mode Quality Control of Oxygen, Nitrate, and pH Data on SOCCOM Biogeochemical Profiling Floats. *Frontiers in Marine Science*, *8*. https://doi.org/10.3389/fmars.2021.683207

Nakamura, T., & Awaji, T. (2004). Tidally induced diapycnal mixing in the Kuril Straits and its role in water transformation and transport: A three-dimensional nonhydrostatic model experiment. *Journal of Geophysical Research: Oceans*, *109*(C9). https://doi.org/10.1029/2003JC001850

Nakamura, T., Awaji, T., Hatayama, T., Akitomo, K., Takizawa, T., Kono, T., et al. (2000a). The Generation of Large-Amplitude Unsteady Lee Waves by Subinertial K1 Tidal Flow: A Possible Vertical Mixing Mechanism in the Kuril Straits. Retrieved from https://journals.ametsoc.org/view/journals/phoc/30/7/1520-0485_2000_030_1601_tgolau_2.0.co_2.xml

Nakamura, T., Awaji, T., Hatayama, T., Akitomo, K., & Takizawa, T. (2000b). Tidal Exchange through the Kuril Straits. Retrieved from https://journals.ametsoc.org/view/journals/phoc/30/7/1520-0485_2000_030_1622_tettks_2.0.co_2.xml

Nicholson, D. P., & Feen, M. L. (2017). Air calibration of an oxygen optode on an underwater glider. *Limnology and Oceanography: Methods*, *15*(5), 495–502. https://doi.org/10.1002/lom3.10177

Ogata, T., & Nonaka, M. (2020). Mechanisms of Long-Term Variability and Recent Trend of Salinity Along 137°E. *Journal of Geophysical Research: Oceans*, *125*(2), e2019JC015290. https://doi.org/10.1029/2019JC015290

Pacanowski, R. C., and S. M. Griffies (2000), MOM 3.0 Manual, Technical Report 4, 680 pp., Geophys. Fluid Dyn. Lab., Princeton, N. J. Philander, S. G. H. (1990), El Niño, La Niiña, and the Southern Oscillation, pp. 293, Academic Press, San Diego, Calif.

Pörtner, H. O., & Farrell, A. P. (2008). Physiology and Climate Change. *Science*, *322*(5902), 690–692. https://doi.org/10.1126/science.1163156

Pozo Buil, M., & Di Lorenzo, E. (2017). Decadal dynamics and predictability of oxygen and subsurface tracers in the California Current System. *Geophysical Research Letters*, *44*(9), 4204–4213. https://doi.org/10.1002/2017GL072931

Reid, J. L. (1997). On the total geostrophic circulation of the pacific ocean: flow patterns, tracers, and transports. *Progress in Oceanography*, *39*(4), 263–352. https://doi.org/10.1016/S0079-6611(97)00012-8

Roemmich, D., & Gilson, J. (2009). The 2004–2008 mean and annual cycle of temperature, salinity, and steric height in the global ocean from the Argo Program. *Progress in Oceanography*, *82*(2), 81–100. https://doi.org/10.1016/j.pocean.2009.03.004

Sampaio, E., Santos, C., Rosa, I. C., Ferreira, V., Pörtner, H.-O., Duarte, C. M., et al. (2021). Impacts of hypoxic events surpass those of future ocean warming and acidification. *Nature Ecology & Evolution*, *5*(3), 311–321. https://doi.org/10.1038/s41559-020-01370-3

Sasaki, H., Nonaka, M., Masumoto, Y., Sasai, Y., Uehara, H., & Sakuma, H. (2008). An Eddy-Resolving Hindcast Simulation of the Quasiglobal Ocean from 1950 to 2003 on the Earth Simulator. In K. Hamilton & W. Ohfuchi (Eds.), *High Resolution Numerical Modelling of the Atmosphere and Ocean* (pp. 157–185). New York, NY: Springer. https://doi.org/10.1007/978-0-387-49791-4_10

Sasano, D., Takatani, Y., Kosugi, N., Nakano, T., Midorikawa, T., & Ishii, M. (2015). Multidecadal trends of oxygen and their controlling factors in the western North Pacific. *Global Biogeochemical Cycles*, *29*(7), 935–956. https://doi.org/10.1002/2014GB005065

945 Sasano, D., Takatani, Y., Kosugi, N., Nakano, T., Midorikawa, T., & Ishii, M. (2018). Decline and
946 Bidecadal Oscillations of Dissolved Oxygen in the Oyashio Region and Their Propagation to the
947 Western North Pacific. *Global Biogeochemical Cycles*, *32*(6), 909–931.
948 https://doi.org/10.1029/2017GB005876
949 Schmidtko, S., Stramma, L., & Visbeck, M. (2017). Decline in global oceanic oxygen content during
950 the past five decades. *Nature*, *542*(7641), 335–339. https://doi.org/10.1038/nature21399
951 Sharp, J. D., Fassbender, A. J., Carter, B. R., Johnson, G. C., Schultz, C., Dunne, J. P. (2022). GOBAI-
952 O_2: A Global Gridded Monthly Dataset of Ocean Interior Dissolved Oxygen Concentrations Based on
953 Shipboard and Autonomous Observations (NCEI Accession 0259304). NOAA National Centers for
954 Environmental Information. Dataset. https://doi.org/10.25921/z72m-yz67.
955 Sharp, J. D., Fassbender, A. J., Carter, B. R., Johnson, G. C., Schultz, C., & Dunne, J. P. (2023).
956 GOBAI-O_2: temporally and spatially resolved fields of ocean interior dissolved oxygen over nearly 2
957 decades. *Earth System Science Data*, *15*(10), 4481–4518. https://doi.org/10.5194/essd-15-4481-2023
958 Stramma, L., Johnson, G. C., Sprintall, J., & Mohrholz, V. (2008). Expanding Oxygen-Minimum
959 Zones in the Tropical Oceans. *Science*, *320*(5876), 655–658. https://doi.org/10.1126/science.1153847
960 Stramma, L., Schmidtko, S., Bograd, S. J., Ono, T., Ross, T., Sasano, D., & Whitney, F. A. (2020).
961 Trends and decadal oscillations of oxygen and nutrients at 50 to 300 m depth in the equatorial
962 and North Pacific. *Biogeosciences*, *17*(3), 813–831. https://doi.org/10.5194/bg-17-813-2020
963 Stramma, L., & Schmidtko, S. (2021). Tropical deoxygenation sites revisited to investigate oxygen
964 and nutrient trends. *Ocean Science*, *17*(3), 833–847. https://doi.org/10.5194/os-17-833-2021
965 Suga, T., Takei, Y., & Hanawa, K. (1997). Thermostad Distribution in the North Pacific Subtropical
966 Gyre: The Central Mode Water and the Subtropical Mode Water. Retrieved from
967 https://journals.ametsoc.org/view/journals/phoc/27/1/1520-
968 0485_1997_027_0140_tditnp_2.0.co_2.xml

969 Suga, T., Motoki, K., Aoki, Y., & Macdonald, A. M. (2004). The North Pacific Climatology of Winter
970 Mixed Layer and Mode Waters. Retrieved from
971 https://journals.ametsoc.org/view/journals/phoc/34/1/1520-
972 0485_2004_034_0003_tnpcow_2.0.co_2.xml
973 Takatani, Y., Sasano, D., Nakano, T., Midorikawa, T., & Ishii, M. (2012). Decrease of dissolved
974 oxygen after the mid-1980s in the western North Pacific subtropical gyre along the 137°E repeat
975 section. *Global Biogeochemical Cycles*, *26*(2). https://doi.org/10.1029/2011GB004227
976 Takeshita, Y., Martz, T. R., Johnson, K. S., Plant, J. N., Gilbert, D., Riser, S. C., et al. (2013). A
977 climatology-based quality control procedure for profiling float oxygen data. *Journal of Geophysical*
978 *Research: Oceans*, *118*(10), 5640–5650. https://doi.org/10.1002/jgrc.20399
979 Udaya Bhaskar, T. V. S., Sarma, V. V. S. S., & Pavan Kumar, J. (2021). Potential Mechanisms
980 Responsible for Spatial Variability in Intensity and Thickness of Oxygen Minimum Zone in the Bay
981 of Bengal. *Journal of Geophysical Research: Biogeosciences*, *126*(6), e2021JG006341.
982 https://doi.org/10.1029/2021JG006341
983 Winkler, L. W. (1888). Die Bestimmung des im Wasser gelösten Sauerstoffes. *Berichte Der Deutschen*
984 *Chemischen Gesellschaft*, *21*(2), 2843–2854. https://doi.org/10.1002/cber.188802102122
985 Wolf, M. K., Hamme, R. C., Gilbert, D., Yashayaev, I., & Thierry, V. (2018). Oxygen Saturation
986 Surrounding Deep Water Formation Events in the Labrador Sea From Argo-O_2 Data. *Global*
987 *Biogeochemical Cycles*, *32*(4), 635–653. https://doi.org/10.1002/2017GB005829
988 Xu, L., Wang, K., & Wu, B. (2022). Weakening and Poleward Shifting of the North Pacific Subtropical
989 Fronts from 1980 to 2018. *Journal of Physical Oceanography*, *52*(3), 399-417.
990 https://doi.org/https://doi.org/10.1175/JPO-D-21-0170.1

991 Yang, H., Lohmann, G., Krebs-Kanzow, U., Ionita, M., Shi, X., Sidorenko, D., et al. (2020). Poleward
992 Shift of the Major Ocean Gyres Detected in a Warming Climate. *Geophysical Research Letters*, *47*(5),
993 e2019GL085868. https://doi.org/10.1029/2019GL085868
994 Yasuda, I. (2004). North Pacific Intermediate Water: Progress in SAGE (SubArctic Gyre Experiment)
995 and Related Projects. *Journal of Oceanography*, *60*(2), 385–395.
996 https://doi.org/10.1023/B:JOCE.0000038344.25081.42
997 You, Y. (2003). The pathway and circulation of North Pacific Intermediate Water. *Geophysical*
998 *Research Letters*, *30*(24). https://doi.org/10.1029/2003GL018561
999
1000
1001